Effective atomic number image determination with an energy-resolving photon-counting detector using polychromatic X-ray attenuation by correcting for the beam hardening effect and detector response

doi: https://doi.org/10.1016/j.apradiso.2021.109617

Title

Effective atomic number image determination with an energy-resolving photon-counting detector using polychromatic X-ray attenuation by correcting for the beam hardening effect and detector response

Author names

Natsumi Kimoto[1)]	natsumi.kimoto.0717@gmail.com
Hiroaki Hayashi[1)]	hayashi.hiroaki@staff.kanazawa-u.ac.jp
Takumi Asakawa[1)]	takumiasakawa.24@gmail.com
Cheonghae Lee[1)]	lee.cheonghae.1999@gmail.com
Takashi Asahara[1,2)]	takashi.asahara.111@gmail.com
Tatsuya Maeda[1)]	tatsuya.maeda.1108@gmail.com
Sota Goto[1,3)]	gotosota.19960221@gmail.com
Yuki Kanazawa[4)]	yk@tokushima-u.ac.jp
Akitoshi Katsumata[5)]	kawamata@dent.asahi-u.ac.jp
Shuichiro Yamamoto[6)]	s.yamamoto@job-image.com
Masahiro Okada[6)]	maple@mth.biglobe.ne.jp

Affiliation

1) Graduate School of Medical Sciences, Kanazawa University,
   Ishikawa, 920-0942, Japan
   TEL: +81-76-265-2523
2) Division of Radiology, Medical Support Department, Okayama University Hospital
   Okayama, 700-8558, Japan
   TEL: +81-86-223-7151
3) National Metrology Institute of Japan, National Institute of Advanced Industrial Science and Technology
   Ibaraki, 305-8568, Japan
   TEL: +81-80-6347-5109
4) Graduate School of Biomedical Sciences, Tokushima University
   Tokushima, 770-8503, Japan
   TEL: +81-88-633-9054
5) Department of Oral Radiology, Asahi University
   Gifu, 501-0223, Japan
   TEL: +81-58-329-1111
6) JOB CORPORATION
   Kanagawa, 222-0033, Japan
   TEL: +81-45-473-0113

Corresponding Author
Hiroaki Hayashi[1) hayashi.hiroaki@staff.kanazawa-u.ac.jp

Keywords (3–5)
photon-counting; detector response; beam hardening effect; effective atomic number

Abstract (not more than 80 words)
In this study, we propose an effective atomic number (Z_{eff}) determination method based on a photon-counting technique. The proposed method can correct for the effects of beam hardening and the detector response based on polychromatic X-rays to allow high accuracy material identification. To demonstrate the effectiveness of our method, the procedure was applied to X-ray images acquired by a prototype energy-resolving photon-counting detector and we obtained an Z_{eff} image with accuracy of $Z_{\mathrm{eff}} \pm 0.5$ regardless of the mass thickness.

Acknowledgments
This study was partially supported by JSPS KAKENHI Grant Number JP18K09734 and a Kurata Grant awarded by the Hitachi Global Foundation.

Main Text

1. Introduction

X-ray images play important roles in medical diagnosis and non-invasive inspection. In the conventional evaluation of an image, we focus on the contrast represented by the differences in X-ray attenuation depending on the material. However, the conventional method has limitations, particularly the problem that low contrast materials may not be visually distinguished from each other. To solve this limitation and greatly enhance the evaluation level, we aimed to develop a novel X-ray imaging system that can provide quantitative information, such as an effective atomic number (Z_{eff}) image.

Direct and indirect type energy integrating detectors (EID) [Spekowius and Wendler, 2006, Samei and Flynn, 2003] are used at present in X-ray imaging systems. Well-known types of imaging detectors such as analog detectors (X-ray film), computed radiography [Rowlands, 2002], and digital radiography systems [Korner et al., 2007] are employed as EIDs, where the signal output is proportional to the total amount of X-ray energy absorbed. This energy integration mode makes it difficult to analyze the energy of each X-ray, and thus new approaches have been developed. For example, a dual-energy technique [Alvarez and Macovski, 1979] was tested that uses X-ray tubes with different voltages. In addition, an energy-resolving photon-counting detector (ERPCD) [Taguchi et al., 2013, Leng et al., 2019, Willemink et al., 2018] has been developed that uses a direct-conversion-type semiconductor detector and it is a promising alternative to EID. The ERPCD can analyze X-rays individually and discriminate the X-ray energy by using several energy thresholds. The ERPCD allows the simultaneous analysis of multiple X-ray energies because of its energy discriminating ability even if irradiation with a single polychromatic X-ray is applied.

In order to maximize the functionality and performance of an actual ERPCD, it should be considered that not all X-rays are completely absorbed by the ERPCD, where this incomplete absorption is caused by the physical interactions between incident X-rays and detector materials [Reza, 2018, Hayashi et al., 2017, Hayashi et al., 2021, Taguchi et al., 2018] and electric phenomena such as the charge sharing effect [Trueb et al., 2017, Otfinowski, 2018, Zambon et al., 2018] and energy resolution [Hsieh et al., 2018]. In particular, the response function including these effects should be considered when analyzing X-ray signals in each energy bin. In general, the effect of the detector response can be corrected by an unfolding procedure [Maeda et al., 2005], where the X-ray spectra are measured using a multi-channel analyzer with a number of energy bins. However, it is difficult to apply this conventional technique to current ERPCDs with only a few energy bins. Furthermore, precise analysis of Z_{eff} needs to consider the change in the effective energy in each energy bin caused by the beam hardening effect of an object [Brooks and Di Chiro, 1976]. In our previous study [Kimoto et al., 2017], we determined the impact and correction procedure for the beam hardening effect related to soft tissue (Z_{eff} = 7.0) and aluminum (Z_{eff} = 13.0), but this method should be improved for application to objects comprising various Z_{eff} values and thicknesses.

Several practical algorithms have been proposed for determining Z_{eff} and/or identifying materials [Wang et al., 2011, Fredenberg et al., 2013, Iramina et al., 2018, Yamashita et al., 2014, Dong et al., 2019, Sellerer et al., 2019, Rinkel et al., 2011]. For example, Wang et al. proposed a practical material decomposition procedure based on the relationship between the products of the linear attenuation coefficient and material thickness (μt) for two different energies, but they did not correct for the beam hardening effect and detector response, and they successfully decomposed different materials by comparing them with reference materials [Wang et al., 2011]. This method can be applied only in limited situations because appropriate reference samples are required for all different Z_{eff} values and thicknesses. By contrast, our approach that corrects for the aforementioned phenomena can be applied to general objects without reference materials.

In this study, we propose a novel method for correcting both the beam hardening effect and detector response without Z_{eff} or thickness information for an object when using polychromatic X-rays. After these effects are corrected for in an appropriate manner, the signals related to each energy bin can be treated as a monochromatic X-ray and Z_{eff} can be analyzed using an accurate value for μ [Hubbell, 1982]. Our study is based on a Cadmium Zinc Telluride (CZT) detector, which is considered feasible for use as an ERPCD in medical applications [Scheiber and Giakos, 2001].

2. Materials and Methods

2.1 Novel algorithm for determining Z_{eff}

In this study, we propose a method that can determine the Z_{eff} value for an object by analyzing the linear attenuation coefficient "μ" depending on the X-ray energy. First, we explain the basic concept applied in our method using monochromatic X-rays, which correspond to the mean energies weighted with a spectrum, as described in section 2.1.1. We then extend our method to a more realistic situation where polychromatic X-rays are detected by ERPCD, as described in section 2.1.2. Polychromatic X-rays can be regarded as a monochromatic X-ray by applying a correction procedure where the beam hardening effect and detector response are corrected simultaneously.

To explain the proposed method, we define the polychromatic X-ray distribution as an expression of $\mathbf{\Phi}(E)$, where E is the energy of an X-ray, which is then reproduced using a semi-empirical formula [Birch and Marshall, 1979]. We set the X-ray spectrum at a tube voltage of 50 kV (tungsten target with a total filtration of 2.5 mm aluminum) with an interval of 0.2 keV:

$$\mathbf{\Phi} = \begin{pmatrix} \Phi(0\ \mathrm{keV}) \\ \Phi(0.2\ \mathrm{keV}) \\ \vdots \\ \Phi(E) \\ \vdots \\ \Phi(50\ \mathrm{keV}) \end{pmatrix}. \quad (1)$$

The distributions of X-rays that are incident and that after penetrating an object are defined as $\mathbf{\Phi}_{\mathrm{i}}(E)$ and $\mathbf{\Phi}_{\mathrm{p}}(E)$, respectively. We set the low, middle, and high energy bins in ERPCD as 20–32 keV, 32–40 keV, and 40–50 keV, respectively, and the mean energy weighted using a spectrum $\bar{E}$ in each energy bin is calculated as:

$$\bar{E} = \frac{\sum_{E_1}^{E_2} \mathbf{\Phi}_{\mathrm{i}}(E)E}{\sum_{E_1}^{E_2} \mathbf{\Phi}_{\mathrm{i}}(E)}, \quad (2)$$

where E_1 and E_2 are the lower and upper energies of each energy bin, respectively. Consequently, the $\bar{E}$ values for the low, middle, and high energy bins are 26.9 keV, 35.8 keV, and 43.4 keV, respectively.

2.1.1 Monochromatic X-ray

Next, we describe our method based on the assumption that monochromatic X-rays with ideal X-ray spectra can be obtained. Therefore, we treat the $\bar{E}$ value of each energy bin in the X-ray spectrum as a monochromatic X-ray. When an object is measured, the X-ray attenuation μt is calculated for $\bar{E}$ as:

$$\mu t = \mu(\bar{E})t = \ln\left(\frac{\mathbf{\Phi}_{\mathrm{i}}(\bar{E})}{\mathbf{\Phi}_{\mathrm{p}}(\bar{E})}\right), \tag{3}$$

where μ and t are the linear attenuation coefficient and material thickness, respectively. In our system, we defined μt values related to the low, middle, and high energy bins as $\mu_{\mathrm{low}}t$, $\mu_{\mathrm{middle}}t$, and $\mu_{\mathrm{high}}t$, respectively. We focus on μ in μt because μ is related to Z_{eff} [Knoll, 2000]. In order to derive μ from μt, the following calculations are performed:

$$\mu_{\mathrm{low}}{}^{\dagger} = \frac{\mu_{\mathrm{low}}t}{\sqrt{(\mu_{\mathrm{low}}t)^2+(\mu_{\mathrm{middle}}t)^2}} = \frac{\mu_{\mathrm{low}}}{\sqrt{\mu_{\mathrm{low}}{}^2+\mu_{\mathrm{middle}}{}^2}}, \tag{4-1}$$

$$\mu_{\mathrm{high}}{}^{\dagger} = \frac{\mu_{\mathrm{high}}t}{\sqrt{(\mu_{\mathrm{high}}t)^2+(\mu_{\mathrm{middle}}t)^2}} = \frac{\mu_{\mathrm{high}}}{\sqrt{\mu_{\mathrm{high}}{}^2+\mu_{\mathrm{middle}}{}^2}}, \tag{4-2}$$

where $\mu_{\mathrm{low}}{}^{\dagger}$ and $\mu_{\mathrm{high}}{}^{\dagger}$ are the normalized linear attenuation coefficients. In order to derive Z_{eff} from these values, we use reference curves obtained from a well-known database [Hubbell, 1982]. This reference curve allows us to determine Z_{eff} using the experimentally determined normalized linear attenuation coefficients. It should be noted that the validity of this analysis is limited to the use of a monochromatic X-ray.

2.1.2 Polychromatic X-rays folded with the response function of a multi-pixel type ERPCD

In the following, we explain our method for determining Z_{eff} using polychromatic X-rays by considering the response of a multi-pixel type ERPCD. It should be noted that the energy signals in each energy bin cannot be treated as monochromatic X-rays that have the same mean energies weighted using a spectrum $\bar{E}$ determined by equation (2) because $\bar{E}$ varies according to the beam hardening effect and detector response. The method used to estimate Z_{eff} for an object by correcting for both effects differs considerably from the analysis of a monochromatic X-ray, and this point is the novel feature of the proposed approach.

Figure 1 shows a schematic illustration of our procedure for determining the Z_{eff} value for an object using reproduced X-ray spectra by employing polychromatic X-rays folded with the detector response. Initially, X-ray spectra detected by an ERPCD under two conditions with and without objects are prepared as shown on the left in Fig. 1. In order to calculate the attenuation factors for polychromatic X-rays, as shown in Fig. 1(a), the intensities of monochromatic X-rays in equation (3) are replaced by those for polychromatic X-rays folded with the detector response as follows:

$$(\mu t)_{\mathrm{meas}} = \ln\left(\frac{\sum_{E_1}^{E_2}\mathbf{R}^{(1)}\mathbf{R}^{(2)}\mathbf{\Phi}_{\mathrm{i}}(E)}{\sum_{E_1}^{E_2}\mathbf{R}^{(1)}\mathbf{R}^{(2)}\mathbf{\Phi}_{\mathrm{p}}(E)}\right), \tag{5}$$

where $(\mu t)_{\mathrm{meas}}$ is the attenuation factor obtained from an energy bin, and $\mathbf{R}^{(1)}\mathbf{R}^{(2)}\mathbf{\Phi}_{\mathrm{i}}(E)$ and $\mathbf{R}^{(1)}\mathbf{R}^{(2)}\mathbf{\Phi}_{\mathrm{p}}(E)$ are the intensities of the X-ray spectra detected by the ERPCD under the two conditions without and with objects, respectively. The reproduced X-ray spectrum expressed by $\mathbf{R}^{(1)}\mathbf{R}^{(2)}\mathbf{\Phi}(E)$ is derived by folding the ideal X-ray spectrum $\mathbf{\Phi}$ with the detector response $\mathbf{R}^{(1)}\mathbf{R}^{(2)}$, and the detailed calculation procedure is described in section 2.2. Next, attenuation factors corresponding to the low, middle, and high energy bins are defined as $(\mu_{\mathrm{low}}t)_{\mathrm{meas}}$, $(\mu_{\mathrm{middle}}t)_{\mathrm{meas}}$, and $(\mu_{\mathrm{high}}t)_{\mathrm{meas}}$, respectively. At this time, $(\mu t)_{\mathrm{meas}}$ is distorted by the beam hardening effect and detector response, so these effects should be corrected to determine the true Z_{eff}.

For clarity, we define a tentative Z_{eff} as "Z_{tent}," which is used to calculate a correction curve for the beam hardening effect and detector response. The correction is then performed, where $(\mu_{\text{low}}t)_{\text{meas}}$, $(\mu_{\text{middle}}t)_{\text{meas}}$, and $(\mu_{\text{high}}t)_{\text{meas}}$ are corrected to $(\mu_{\text{low}}t)_{\text{cor}}$, $(\mu_{\text{middle}}t)_{\text{cor}}$, and $(\mu_{\text{high}}t)_{\text{cor}}$, respectively, and the detailed correction procedure is described in section 2.3. For example, by changing Z_{tent} to 5.0, 6.0, …, and 15.0, the corrections related to the Z_{tent} values are applied to each $(\mu t)_{\text{meas}}$, as shown in Fig. 1(b). Finally, based on the same algorithm used for the analysis of Z_{eff} using monochromatic X-rays, Z_{eff} is determined from ${\mu_{\text{high}}}^{\dagger}$. The Z_{eff} values obtained are labeled as "$Z_{\text{eff,high}}$" values, as shown in Fig. 1(c). In the same manner, the $Z_{\text{eff,low}}$ values are also determined from ${\mu_{\text{low}}}^{\dagger}$. To derive the Z_{eff} value of an object, the $Z_{\text{eff,low}}$ and $Z_{\text{eff,high}}$ values are plotted as a function of Z_{tent}, as shown in Fig. 1(d). The procedure for determining Z_{eff} is as follows. When the derived $Z_{\text{eff,low}}$ and/or $Z_{\text{eff,high}}$ values are the same as Z_{tent}, the corresponding value becomes Z_{eff} for an object. However, if Z_{tent} differs from the Z_{eff} for an object, Z_{tent} does not agree with $Z_{\text{eff,low}}$ and $Z_{\text{eff,high}}$. This solution is clearly determined at the intersection point where the $Z_{\text{eff,low}}$ and/or $Z_{\text{eff,high}}$ curves intersect at the Y = X line ($Z_{\text{eff}} = Z_{\text{tent}}$).

2.2 Procedure for reproducing X-ray spectrum by considering the response of a multi-pixel type ERPCD

Next, we explain the reproduction of an X-ray spectrum obtained with a multi-pixel type ERPCD. Figure 2 compares an ideal case X-ray spectrum with an actual spectrum where the response function of the ERPCD is considered. Figure 2(a) shows an ideal case where all of the energies of the incident X-rays are absorbed completely by the detector. Using the response function represented by an identity matrix "**I**," the X-ray spectrum obtained is calculated by the matrix operation $\mathbf{I\Phi}$ (= $\mathbf{\Phi}$). In order to obtain the X-ray spectrum by considering the response function of ERPCD, the two different phenomena $\mathbf{R}^{(1)}$ and $\mathbf{R}^{(2)}$ should also be considered. Figure 2(b.1) shows $\mathbf{R}^{(1)}$ where we consider the transportation of secondary produced X-rays caused by the photoelectric effect and photons scattered due to the Compton scattering effect. Figure 2(b.2) shows $\mathbf{R}^{(2)}$ where the charge sharing effect and energy resolution are considered. The X-ray spectrum obtained under the actual conditions can then be reproduced by the matrix operation $\mathbf{R}^{(1)}\mathbf{R}^{(2)}\mathbf{\Phi}$.

To calculate $\mathbf{R}^{(1)}$, we simulate the interaction between the incident X-rays and monolithic detector materials using the Monte-Carlo simulation code EGS5 [Hirayama and Namito, 2005]. The detector materials comprise CZT at a ratio of Cd:Zn:Te = 0.9:0.1:1.0 with a density of 5.8 g/cm^3 and the outer size of the monolithic detector material is set as 10 mm × 10 mm × 1.5 mm. The response function is defined as the normalized spectra for a region measuring 200 μm × 200 μm. We calculate the response function with 10^6 photons incident to the center pixel, and the total irradiation area is 5 × 5 pixels in order to establish equilibrium for the secondary produced radiation [Reza, 2018, Hayashi et al., 2017, Hayashi et al., 2021]. A two-dimensional matrix $\mathbf{R}^{(1)}$ is constructed of elements corresponding to 0–140 keV monochromatic incident X-rays. One 80-keV monochromatic X-ray vector element in $\mathbf{R}^{(1)}$ is illustrated as an example in Fig. 3(a). The red line represents the full energy peak (FEP), which appears when all of the incident X-ray energy is absorbed completely by the pixel of interest. The blue area represents partially absorbed events, and some intense peaks are observed at 23–32 keV and 48–57 keV. The photoelectric effect mainly occurs when the X-rays are incident to the pixel, and thus the characteristic X-rays produced subsequently are considered. When we consider the effects of the characteristic X-rays on the pixel of interest, it is possible that the characteristic X-rays may escape the pixel and this phenomenon causes the existence of escape peaks (EPs) at 48–57 keV. In addition, the peaks at 23–32 keV can be explained as follows. When the X-ray is incident to the adjacent pixels and the characteristic X-rays of Cd (23–27 keV) and Te (27–32 keV) are generated, it is possible that these characteristic X-rays become incident to the pixel of interest. It should be noted that the characteristic X-ray peaks of Cd and Te are constant regardless of the energy of the incident X-rays, whereas the escape peaks vary according to the energy of the incident X-rays [Reza, 2018, Hayashi et al., 2017, Hayashi et al., 2021]. It should be noted that the effect of Zn on the response function is negligibly small because the amount of Zn only comprises 1/20th of the material's composition.

The $\mathbf{R}^{(2)}$ value includes the charge sharing effect $\mathbf{r}^{(2,c)}$ and energy resolution $\mathbf{r}^{(2,e)}$. During the charge collection process within the detector materials, electrons in the charge cloud undergo a diffusion process and drift due to the electric field. In addition, not all of the charges are collected by the pixel of interest and some charges escape to adjacent pixels, which is called the charge sharing effect. The vector elements of $\mathbf{r}^{(2,c)}$ are presented in Fig. 3(b.1). $\mathbf{r}^{(2,c)}$ has two components: comprising the peak and the other part described by a flat distribution [Trueb et al., 2017, Otfinowski, 2018, Zambon et al., 2018]. The ratios of the peak and the other part are determined as 35% and 65%, respectively, when reproducing the response of our prototype ERPCD. The energy resolution $\mathbf{r}^{(2,e)}$ is 5% for the 80-keV monochromatic X-ray and it is optimized to reproduce the characteristic X-ray peaks of Cd and Te. The energy dependence of the resolution is also considered, where the effect is expressed using the Gaussian function, with the standard deviation proportional to the square root of the energy [Knoll, 2000]. Using $\mathbf{r}^{(2,c)}$ and $\mathbf{r}^{(2,e)}$, $\mathbf{R}^{(2)}$ is derived as shown in Fig. 3(b), which illustrates the broad peak at around 80 keV and the flat distribution.

Next, we explain the procedure employed to reproduce the actual X-ray spectrum. First, as shown in Fig. 4(a), the ideal X-ray spectrum $\mathbf{\Phi}$ is obtained using a semi-empirical formula [Birch and Marshall, 1979]. We set the tube voltage at 50 kV with an interval of 0.2 keV:

$$\mathbf{\Phi} = \begin{pmatrix} \Phi(0\ \ \text{keV}) \\ \Phi(0.2\ \ \text{keV}) \\ \vdots \\ \Phi(E') \\ \vdots \\ \Phi(50\ \ \text{keV}) \end{pmatrix} = \begin{pmatrix} \Phi_1 \\ \Phi_2 \\ \vdots \\ \Phi_\mathrm{j} \\ \vdots \\ \Phi_{251} \end{pmatrix}, \tag{6}$$

where E' is the incident X-ray energy. The element of this vector is expressed as "Φ_j." Then, we reproduce the detector response $\mathbf{R}^{(1)}\mathbf{R}^{(2)}$ using matrixes $\mathbf{R}^{(1)}$ and $\mathbf{R}^{(2)}$. $\mathbf{R}^{(1)}$ comprises the elements of $\mathbf{R}^{(1)}_{E'}$ corresponding to various incident X-ray energies E'. Then, $\mathbf{R}^{(1)}_{E'}$ is expressed as $\{\mathbf{R}^{(1)}_{\mathrm{i},1}, \mathbf{R}^{(1)}_{\mathrm{i},2}, \mathbf{R}^{(1)}_{\mathrm{i,j}}, \ldots, \mathbf{R}^{(1)}_{\mathrm{i},251}\}$ where the corresponding response energy is the i-th element. A similar notation rule for $\mathbf{R}^{(1)}$ is applied to $\mathbf{R}^{(2)}$, i.e., the matrix $\mathbf{R}^{(2)}$ has the elements of $\mathbf{R}^{(2)}_{E'}$. In the process employed to derive $\mathbf{R}^{(1)}\mathbf{R}^{(2)}$, the element of $\mathbf{R}^{(1)}$ in the i-th row and k-th column is expressed as $\mathrm{R}^{(1)}_{\mathrm{i,k}}$, and the element of $\mathbf{R}^{(2)}$ in the k-th row and j-th column is expressed as $\mathrm{R}^{(2)}_{\mathrm{k,j}}$. Then, the response of $\mathbf{R}^{(1)}\mathbf{R}^{(2)}$ can be expressed as:

$$\mathbf{R}^{(1)}\mathbf{R}^{(2)} = \begin{pmatrix} \mathbf{R}^{(1)}_{0\ \mathrm{keV}} \\ \mathbf{R}^{(1)}_{0.2\ \mathrm{keV}} \\ \vdots \\ \mathbf{R}^{(1)}_{E'} \\ \vdots \\ \mathbf{R}^{(1)}_{50\ \mathrm{keV}} \end{pmatrix} \begin{pmatrix} \mathbf{R}^{(2)}_{0\ \mathrm{keV}} \\ \mathbf{R}^{(2)}_{0.2\ \mathrm{keV}} \\ \vdots \\ \mathbf{R}^{(2)}_{E'} \\ \vdots \\ \mathbf{R}^{(2)}_{50\ \mathrm{keV}} \end{pmatrix}$$

$$= \begin{pmatrix} \mathrm{R}^{(1)}_{1,1} & \mathrm{R}^{(1)}_{1,2} & \cdots & \cdots & \cdots & \mathrm{R}^{(1)}_{1,251} \\ \mathrm{R}^{(1)}_{2,1} & \ddots & \vdots & \vdots & \vdots & \vdots \\ \vdots & \vdots & \ddots & \vdots & \vdots & \vdots \\ \vdots & \vdots & \vdots & \mathrm{R}^{(1)}_{\mathrm{i,k}} & \vdots & \vdots \\ \vdots & \vdots & \vdots & \vdots & \ddots & \vdots \\ \mathrm{R}^{(1)}_{251,1} & \cdots & \cdots & \cdots & \cdots & \mathrm{R}^{(1)}_{251,251} \end{pmatrix} \begin{pmatrix} \mathrm{R}^{(2)}_{1,1} & \mathrm{R}^{(2)}_{1,2} & \cdots & \cdots & \cdots & \mathrm{R}^{(2)}_{1,251} \\ \mathrm{R}^{(2)}_{2,1} & \ddots & \vdots & \vdots & \vdots & \vdots \\ \vdots & \vdots & \ddots & \vdots & \vdots & \vdots \\ \vdots & \vdots & \vdots & \mathrm{R}^{(2)}_{\mathrm{k,j}} & \vdots & \vdots \\ \vdots & \vdots & \vdots & \vdots & \ddots & \vdots \\ \mathrm{R}^{(2)}_{251,1} & \cdots & \cdots & \cdots & \cdots & \mathrm{R}^{(2)}_{251,251} \end{pmatrix}$$

$$= \begin{pmatrix} \mathrm{R}^{(1,2)}_{1,1} & \mathrm{R}^{(1,2)}_{1,2} & \cdots & \cdots & \cdots & \mathrm{R}^{(1,2)}_{1,251} \\ \mathrm{R}^{(1,2)}_{2,1} & \ddots & \vdots & \vdots & \vdots & \vdots \\ \vdots & \vdots & \ddots & \vdots & \vdots & \vdots \\ \vdots & \vdots & \vdots & \mathrm{R}^{(1,2)}_{\mathrm{i,j}} & \vdots & \vdots \\ \vdots & \vdots & \vdots & \vdots & \ddots & \vdots \\ \mathrm{R}^{(1,2)}_{251,1} & \cdots & \cdots & \cdots & \cdots & \mathrm{R}^{(1,2)}_{251,251} \end{pmatrix}, \tag{7}$$

where

$$\mathrm{R}^{(1,2)}_{\mathrm{i,j}} = \textstyle\sum_{\mathrm{k}} \mathrm{R}^{(1)}_{\mathrm{i,k}}\, \mathrm{R}^{(2)}_{\mathrm{k,j}}.$$

$\mathbf{R}^{(1)}\mathbf{R}^{(2)}$ is a matrix comprising 251 × 251 elements, and we define a row and column as i and j, respectively. The element $\mathbf{R}^{(1)}\mathbf{R}^{(2)}$ in the i-th row and j-th column is expressed as $\mathrm{R}^{(1,2)}_{\mathrm{i,j}}$. Figure 4(b) shows a two-dimensional color map of $\mathbf{R}^{(1)}\mathbf{R}^{(2)}$. The response related to the full energy peaks (FEPs) is shown along the diagonal line and the energy resolution affects the sharpness of the peaks. The characteristic X-rays of Cd and Te are observed around 23 keV. Escape peaks (EPs) are represented by diagonal lines where the highest value is 27 keV. The charge sharing effect causes an increase in the intensities in the low energy region.

By using $\mathbf{\Phi}$ and $\mathbf{R}^{(1)}\mathbf{R}^{(2)}$, we can reproduce the X-ray spectrum $\mathbf{R}^{(1)}\mathbf{R}^{(2)}\mathbf{\Phi}$ with the following calculations:

$$\mathbf{R}^{(1)}\mathbf{R}^{(2)}\mathbf{\Phi} = \begin{pmatrix} \mathrm{R}^{(1,2)}_{1,1} & \mathrm{R}^{(1,2)}_{1,2} & \cdots & \cdots & \cdots & \mathrm{R}^{(1,2)}_{1,251} \\ \mathrm{R}^{(1,2)}_{2,1} & \ddots & \vdots & \vdots & \vdots & \vdots \\ \vdots & \vdots & \ddots & \vdots & \vdots & \vdots \\ \vdots & \vdots & \vdots & \mathrm{R}^{(1,2)}_{\mathrm{i,j}} & \vdots & \vdots \\ \vdots & \vdots & \vdots & \vdots & \ddots & \vdots \\ \mathrm{R}^{(1,2)}_{251,1} & \cdots & \cdots & \cdots & \cdots & \mathrm{R}^{(1,2)}_{251,251} \end{pmatrix} \begin{pmatrix} \Phi_1 \\ \Phi_2 \\ \vdots \\ \Phi_{\mathrm{j}} \\ \vdots \\ \Phi_{251} \end{pmatrix}$$

$$= \begin{pmatrix} \sum_{\mathrm{j}} \mathrm{R}^{(1,2)}_{1,\mathrm{j}}\, \Phi_{\mathrm{j}} \\ \sum_{\mathrm{j}} \mathrm{R}^{(1,2)}_{2,\mathrm{j}}\, \Phi_{\mathrm{j}} \\ \vdots \\ \sum_{\mathrm{j}} \mathrm{R}^{(1,2)}_{\mathrm{i,j}}\, \Phi_{\mathrm{j}} \\ \vdots \\ \sum_{\mathrm{j}} \mathrm{R}^{(1,2)}_{251,\mathrm{j}}\, \Phi_{\mathrm{j}} \end{pmatrix}, \tag{8}$$

where

$$\sum_j R^{(1,2)}_{i,j}\,\Phi_j = \sum_j \left(\sum_k R^{(1)}_{i,k}\,R^{(2)}_{k,j}\right)\Phi_j = \sum_{E'} \left(\sum_k R^{(1)}_{i,k}\,R^{(2)}_{k,E'}\right)\Phi(E'),$$

where j is replaced by E'. The reproduced X-ray spectrum $\mathbf{R}^{(1)}\mathbf{R}^{(2)}\mathbf{\Phi}$ is plotted with the X-ray spectrum measured using our prototype ERPCD as shown in Fig. 4(c). $\mathbf{R}^{(1)}\mathbf{R}^{(2)}\mathbf{\Phi}$ is in good agreement with the experimental data measured with our ERPCD [Kimoto et al., 2018]. $\mathbf{R}^{(1)}\mathbf{R}^{(2)}\mathbf{\Phi}$ differs from the incident X-ray spectrum $\mathbf{\Phi}$, where it has two major features comprising relatively large intensities in the low energy region and the presence of the characteristic X-ray peaks of Cd and Te.

2.3 Procedure used to correct for the beam hardening effect and detector response by considering the Z_{eff} value for an object

In the following, we describe the method used to correct for the beam hardening effect and detector response. This method allows us to obtain the true attenuation factor, i.e., a measured attenuation factor $(\mu t)_{\mathrm{meas}}$ is converted into an ideal attenuation factor $(\mu t)_{\mathrm{cor}}$ (see Fig. 1(b)).

In our method, we employ the relationship between the mass thickness ρt and attenuation factor μt, which is calculated for a monochromatic X-ray in $\mathbf{\Phi}$ (see Fig. 5(a)) and polychromatic X-rays in $\mathbf{R}^{(1)}\mathbf{R}^{(2)}\mathbf{\Phi}$ (see Fig. 5(b)). The former case is related to an ideal X-ray spectrum and the latter includes both the beam hardening effect and detector response. The lower and upper energies of an energy bin are defined as E_1 and E_2, respectively, and the mean energy weighted using a spectrum is calculated as $\bar{E}$ using equation (2). Next, $(\mu t)_{\mathrm{cor}}$ is calculated for a monochromatic X-ray using equation (3). Similarly, $(\mu t)_{\mathrm{meas}}$ is calculated for polychromatic X-rays using equation (5). The basic concept applied in the correction procedure involves converting $(\mu t)_{\mathrm{meas}}$ measured for polychromatic X-rays to an ideal $(\mu t)_{\mathrm{cor}}$ for a monochromatic X-ray.

We propose a novel method where the correction curves for various Z_{eff} values can be expressed in a simple manner. The relationship shown between ρt and μt in the lower left panel in Fig. 5 clearly demonstrates that the gradient Δ of $(\mu t)_{\mathrm{cor}}$ for a monochromatic X-ray becomes μ/ρ depending on the Z_{eff} value of an object. To extend the correction to more general Z_{eff} values, we can obtain the relationship between $\rho t \times \mu/\rho$ $(= \mu t)$ for the X-axis and μt for the Y-axis, as shown in the lower right panel in Fig. 5. To obtain these data tables, we use the theoretical data set μ/ρ [Hubbell, 1982], which contains the known values of an object. The calculation can be performed using the same information employed to obtain the relationship between ρt and μt (lower left panel in Fig. 5). The gradient Δ of $(\mu t)_{\mathrm{cor}}$ for a monochromatic X-ray then becomes 1 (Y = X) regardless of the object, and $(\mu t)_{\mathrm{meas}}$ depends on the Z_{eff} value of the object for polychromatic X-rays. If necessary, this procedure allows the generation of correction curves for integer Z_{eff} values but also for various real Z_{eff} values by interpolating the dependence of Z_{eff} on polychromatic X-rays. Corrections can be performed in the direction shown by the blue arrows in the lower right panel in Fig. 5. Figure 5 illustrates a specific case using Z_{eff} = 13.0 but this method can be extended to general cases using various objects with different Z_{eff} values. We apply the method to objects where Z_{eff} = 5.0–15.0 with ρt = 0–150 g/cm^2 at intervals of 0.1 g/cm^2.

Figure 6 shows the relationship between $\rho t \times \mu/\rho$ and μt, where Figs 6(a), 6(b), and 6(c) correspond to the low, middle, and high energy bins, respectively. The solid and broken lines represent monochromatic and polychromatic X-rays, respectively. The broken lines also show data for Z_{eff}s = 5.0, 6.0, …, and 15.0. These plots clearly show that the amount of correction, which is the difference between the solid and broken lines, becomes larger for higher values of Z_{eff}. By comparing the three different energy bins, we can observe that the amount of correction is larger for the lower energy bin than the other two energy bins.

2.4 Example of Z_{eff} image creation using a proto-type ERPCD

Figure 7 shows a schematic illustration of an experimental setup used for obtaining an Z_{eff} image. A multi-pixel type ERPCD (JOB CORPORATION, Japan) was installed in a slit scanning system [Sasaki et al, 2019, Kimoto et al., 2019]. A line sensor comprising CZT was used with outer dimensions of 4 mm × 195 mm × 1.5 mm. The pixel size was 200 μm × 200 μm. An X-ray generator (JOB CORPORATION, Japan) with a tungsten target and total filtration of 2.5 mm aluminum equivalent thickness was used. The distance between the X-ray focus point and ERPCD detector was 650 mm. Objects were placed on a stage made of a thin carbon fiber-reinforced plastic plate. The distance between the X-ray focus point and stage was 400 mm, and that between the stage and ERPCD was 250 mm. In order to reduce contamination from scattered X-rays, two slits were used, with one at the emission port of the X-ray generator and the other above the ERPCD. The X-ray generator and ERPCD were moved synchronously while the objects remained static. The scanning speed of our system could be set between 0.125 and 32.0 mm/s. The tube voltage and tube current were set at 50 kV and 0.5 mA, respectively. The energy bins were set at 20–32 keV, 32–40 keV, and 40–50 keV. Using an image reconstruction processing, two-dimensional intensity maps of the counts measured for each pixel were obtained for the low, middle, and high energy bins, and we designated the image produced as a "count image." In order to demonstrate the feasibility of our system, the following samples with ρt values of 1.0, 5.0, and 10.0 g/cm^2 were measured: acrylic (Z_{eff} = 6.5), aluminum (Z_{eff} = 13.0), and bilayer structures of acrylic and aluminum (Z_{eff} = 10.5, 9.5, and 8.5). In addition, eight dental samples obtained after tooth extraction were measured. The scanning speed was set at 0.125 mm/s for the acrylic, aluminum, and bilayer structures, with a scanning time of 26 min, and 1.6×10^5 photons were obtained per pixel with no absorbing material. For the dental samples, 8.3×10^4 photons were irradiated per pixel at a speed of 0.25 mm/s and measurement time of 13 min. These measurements were acquired at a low count rate, thereby minimizing the pulse pileup effect. A conventional X-ray image that was almost identical to that measured with an EID could be produced with our system. In each pixel, the intensity related to a conventional X-ray image can be calculated by:

$$\text{intensity} \propto \log\left(\overline{E_{\mathrm{low}}} I_{\mathrm{low}} + \overline{E_{\mathrm{middle}}} I_{\mathrm{middle}} + \overline{E_{\mathrm{high}}} I_{\mathrm{high}}\right), \tag{9}$$

where $\overline{E_{\mathrm{low}}}$, $\overline{E_{\mathrm{middle}}}$, and $\overline{E_{\mathrm{high}}}$ are the mean energies weighted using the spectra for the low, middle, and high energy bins, respectively, and I_{low}, I_{middle}, and I_{high} are the pixel values of the count images for each energy bin. The image was represented on a logarithmic scale to ensure that it was the same as the conventional X-ray image measured with an EID. The corresponding Z_{eff} image was analyzed using the count image. To confirm the analyzed Z_{eff}, a region of interest (ROI) measuring 50 × 50 pixels was set at the center of each object and the mean Z_{eff} value was measured. We then compared the Z_{eff} value measured for each object with the theoretical Z_{eff} value.

It is important to check the applicability of an Z_{eff} determination procedure, as shown in the final process (d) in Fig. 1; therefore, we conducted the following additional simulations. Assuming acrylic, aluminum, and bilayer structures with ρt = 5 g/cm^2, the corresponding X-ray spectra $\mathbf{R}^{(1)}\mathbf{R}^{(2)}\mathbf{\Phi}$ were obtained. $(\mu t)_{\mathrm{meas}}$ and $(\mu t)_{\mathrm{cor}}$

were then simulated, and $Z_{\mathrm{eff,low}}$ and $Z_{\mathrm{eff,high}}$ were determined from $\mu_{\mathrm{low}}{}^{\dagger}$ and $\mu_{\mathrm{high}}{}^{\dagger}$ as functions of Z_{tent}. Z_{eff} was then determined with our method. In order to compare these values with the experimental results, the trends in $Z_{\mathrm{eff,high}}$ were extracted from the X-ray images measured for the acrylic, aluminum, and bilayer structures with ρt = 5 g/cm^2 in each case. The analysis procedures shown in Fig. 1(a) to Fig. 1(c) were applied to analyze the experimental X-ray image of the sample, and the obtained $Z_{\mathrm{eff,high}}$ values were generated to obtain a two-dimensional map corresponding to Z_{tent}. The ROI (50 × 50 pixels) was set at the center of each object, and the mean value of $Z_{\mathrm{eff,high}}$ was measured. We then plotted $Z_{\mathrm{eff,high}}$ as a function of Z_{tent} and determined Z_{eff}. Finally, we confirmed the Z_{eff} results and the trends in $Z_{\mathrm{eff,low}}$ and $Z_{\mathrm{eff,high}}$.

3. Results

Figure 8 shows a block diagram of the proposed imaging system. The images shown in this figure are the results for the dental samples measured with our prototype ERPCD. Our system employed count images with and without samples, as shown on the left in Fig. 8. As indicated by the black arrow in the figure, a conventional X-ray image was produced using the count images from the three energy bins for a sample. The whole process used to obtain the Z_{eff} image is shown by red arrows. Corresponding $(\mu t)_{\mathrm{meas}}$ images were prepared using the middle and high energy bins, and $(\mu t)_{\mathrm{cor}}$ images were obtained by correcting for the beam hardening effect and detector response. The processes were applied based on the numeric Z_{tent} values for 5.0, 6.0, …, and 15.0, and 11 corresponding $(\mu t)_{\mathrm{cor}}$ images were calculated. The Z_{eff} value for each pixel was then determined and the Z_{eff} image was represented using a color scale.

Figure 9 shows the typical Z_{eff} analysis results for acrylic, aluminum, and bilayer structures, each with ρt = 5 g/cm^2. The $Z_{\mathrm{eff,low}}$ and $Z_{\mathrm{eff,high}}$ curves are plotted as solid lines. The Z_{eff} value of an object can be determined based on the intersection point of the Y = X line and $Z_{\mathrm{eff,high}}$ curve, and this point is indicated by an arrow. Figure 9(a) shows the simulation results obtained using the procedure described in section 2.4. The intersection points obtained using $Z_{\mathrm{eff,high}}$ are clearly identified for all cases, and the derived Z_{eff} values are in good agreement with the theoretical Z_{eff} values. By contrast, it was difficult to identify an intersection point using $Z_{\mathrm{eff,low}}$, thereby demonstrating that is appropriate to use $Z_{\mathrm{eff,high}}$ for determining the Z_{eff} value of an object. Figure 9(b) shows the experimental results. The trends in the $Z_{\mathrm{eff,high}}$ curves were similar to those in the simulations. The experimental Z_{eff} results agreed well with the simulated results. Therefore, we conclude that our method can determine Z_{eff} correctly.

Figure 10 shows the results produced for images with acrylic, aluminum, and bilayer structures, where Figs. 10(a), 10(b), and 10(c) are the results for objects with ρt = 1.0, 5.0, and 10.0 g/cm^2, respectively. The upper row shows the conditions for different ρt values, the second row from the top shows the thicknesses of the acrylic and aluminum for each sample, the upper figures show the photographs, and the middle figures show conventional X-ray images. The conventional X-ray images were visualized using the integrated values of the energy absorbed in each pixel, and the results show the differences in the X-ray attenuation depending on Z_{eff} and ρt. Comparisons of materials with the same Z_{eff} value demonstrated that the image density decreased as ρt increased. In addition, comparisons of samples with the same ρt and different Z_{eff} values showed that the image density decreased as Z_{eff} increased. The figures at the bottom show Z_{eff} images on a color scale. The mean Z_{eff} values in the ROI and theoretical Z_{eff} values are presented in the bottom row. The theoretical Z_{eff} values for the acrylic, aluminum, and bilayer structures from left to right are 6.5, 13.0, 10.5, 9.5, and 8.5 regardless of ρt [Spiers, 1946]. Most of the experimental Z_{eff} values are in good agreement with the theoretical values. In the cases where the mean values are within the theoretical range of Z_{eff} ± 0.5, the Z_{eff} values are presented in blue. The values outside the theoretical range of Z_{eff} ± 0.5 are presented in red. Our method can produce an appropriate Z_{eff} image for most objects in addition to a conventional X-ray image. However, the aluminum sample with ρt = 10.0 g/cm^2 is the only case where the measured Z_{eff} value is not in good agreement with the theoretical Z_{eff} value. This limitation is discussed in section 4.4.

4. Discussion

4.1 Parameter settings used in the Z_{eff} determination algorithm

In the proposed Z_{eff} determination method, we only use the X-ray attenuation information related to the middle and high energy bins because these energy bins contain highly original X-ray attenuation information. In addition, the X-ray attenuation information related to a low energy bin is only used to create a conventional X-ray image. In the following, we discuss the relationship in detail between the optimization of these energy bins and the influence of the detector response.

In order to correct for the beam hardening effect and detector response in an appropriate manner, various Z_{tent} values are first assumed and the corresponding Z_{eff} values are then obtained. Next, an algorithm is applied that searches for appropriate corrected conditions in the final Z_{eff} determination process, which has the following important role. If the Z_{eff} value of an object can be assumed exactly with an appropriate beam hardening effect and detector response correction, the intersection points related to the $Z_{\mathrm{eff,low}}$ and $Z_{\mathrm{eff,high}}$ curves always denote the true Z_{eff}. However, the pixel values in the actual image data fluctuate due to statistical deviations, so an approach that is robust to statistical deviations is considered advantageous or it would be difficult to determine the true Z_{eff}. To obtain an accurate Z_{eff} value, the trend in the curve must differ significantly from that in the Y = X line. Figure 9(a) compares the trends in the $Z_{\mathrm{eff,low}}$ and $Z_{\mathrm{eff,high}}$ curves, where the intersection point between the Y = X line and $Z_{\mathrm{eff,high}}$ curve is more clearly identified than that with the $Z_{\mathrm{eff,low}}$ curve. The amount of correction is small for $Z_{\mathrm{eff,high}}$ data, so even if Z_{tent} differs greatly from the true Z_{eff} value, the $Z_{\mathrm{eff,high}}$ values obtained do not differ considerably from the true Z_{eff} values. This explains why the trend in $Z_{\mathrm{eff,high}}$ differs significantly from that in the Y = X line over a wide range of Z_{tent} value. By contrast, the trend in the $Z_{\mathrm{eff,low}}$ values is the opposite, where the variation in $Z_{\mathrm{eff,low}}$ depends greatly on Z_{tent} because the low energy bin requires a large amount of correction. Therefore, we conclude that $Z_{\mathrm{eff,high}}$ is better than $Z_{\mathrm{eff,low}}$ for Z_{eff} determination.

Care is required when handling the data obtained from the low energy bin. When high energy X-rays are incident to the ERPCD, incomplete absorption processes can occur, where the corresponding events are recorded in the low energy bin as if they are low energy X-rays. In particular, it is difficult to extract the attenuation information for the original X-ray incidences related to the low energy bin. Indeed, Fig. 4 shows that the difference between $\mathbf{R}^{(1)}\mathbf{R}^{(2)}\mathbf{\Phi}$ and $\mathbf{\Phi}$ is large for the low energy bin, where a high amount of contamination is caused by the characteristic X-rays at 23–32 keV, escape peaks below 28 keV, and the charge sharing effect. We consider that using the low energy bin is not appropriate for determining Z_{eff} and the energy regions employed should be set above 32 keV.

Our method employs three energy bins and in the following, we explain the role of each energy bin and how many energy bins are suitable for medical imaging, which is a target application. The proposed method can correct for the beam hardening effect and detector response without correcting the shape of the measured X-ray spectrum. Our algorithm for producing the Z_{eff} image can operate using two energy bins [Kimoto, 2017] and these two energy bins should be set above 32 keV. In our study, we set the middle and high energy bins as 32–40 keV and 40–50 keV, respectively. However, information in the low energy region of the X-ray spectrum can also be used for image generation, so it should be utilized when generating a conventional X-ray image. We set the low energy bin as 20–32 keV and the corresponding events are employed for generating the conventional X-ray image, as shown in Fig. 8. Based on these considerations, we suggest that an ERPCD system with three energy bins is suitable for X-ray examinations. A method for correcting the detector response to reproduce an original X-ray spectrum was also reported previously [Park et al., 2018, Dreier et al., 2018], where the procedure utilizes hardware processing and a series of signals related to adjacent pixels in the X-ray absorption spectrum is summed to obtain one main pixel [Park et al., 2018]. In addition, a software approach was proposed that uses a model for correcting the detector response [Dreier et al., 2018], where the parameter employed in the model is optimized based on comparison with the measured data. Many energy bins can be employed in this application for industrial uses but a system with few energy bins was not considered, so they did not need to develop a beam hardening correction method. The advantages of our method are that it corrects for the beam hardening effect and detector response simultaneously in the software process.

We aim to implement our system in medical applications where the exposure dose needs to be reduced. We determined that a system with a large number of energy bins would be disadvantageous because this type of system is susceptible to the effects of statistical fluctuations, which will increase as the exposure dose decreases. It is necessary to ensure that the statistical noise is minimized in the image obtained even if the image is acquired at a low dose. An ERPCD system that uses a small number of energy bins can establish an image with smaller statistical fluctuations compared with a system that utilizes many energy bins, and this is important for implementing a medical application using ERPCD.

4.2 Influence of correcting for the beam hardening effect and detector response

In our method, correcting for the beam hardening effect and detector response facilitates precise analysis of Z_{eff}. If these corrections are not applied, we cannot determine Z_{eff} accurately. In order to demonstrate the importance of correcting for both effects, we analyzed the results obtained without performing these corrections for acrylic and aluminum samples with ρt = 5 g/cm^2. Figure 11(a) shows the image obtained without both corrections. Figure 11(b) shows the image obtained after only correcting for the beam hardening effect. Figure 11(c) shows the image obtained after correcting for both effects. The theoretical Z_{eff} values for acrylic and aluminum are 6.5 and 13.0, respectively, but the Z_{eff} values were obtained as 5.9 and 10.0 without both corrections according to Fig. 11(a), which do not agree with the theoretical values. As shown in Fig. 11(b), when only the beam hardening effect was corrected, the Z_{eff} value for acrylic did not change but that for aluminum changed to 10.3, which is slightly closer to the theoretical value. As shown in Fig. 11(c), after correcting for both effects, the Z_{eff} values were obtained as 6.4 for acrylic and 12.8 for aluminum. These values are in good agreement with the theoretical values. These results demonstrate that it is necessary to correct for both effects. In a previous study [Kimoto et al., 2017], we proposed a method for obtaining Z_{eff} values but it has the following limitations: (1) the beam hardening correction assumes that an object has Z_{eff} values around 7.0 or 13.0, i.e., it cannot select an exact Z_{eff} value for the object to use for correction and (2) the method can only be applied to the X-ray spectra obtained, which must be unfolded once using the response function. In the present study, we improved the analysis procedure in order to eliminate these limitations. In particular, the improved procedure can analyze materials by correcting for the beam hardening effect related to Z_{eff} values of 5.0–15.0 without additional information regarding the Z_{eff} values of objects, and the X-ray spectra measured in several energy bins can be analyzed without correcting for the unfolding procedure.

In this study, we applied this method to a two-dimensional image to evaluate Z_{eff}. This method can also be applied to computed tomography, and it is expected to have a great impact on the development of technology that can help to identify materials in a three-dimensional image.

4.3 Future prospects

Our method can obtain a conventional two-dimensional X-ray image and an Z_{eff} image. Evaluations of a conventional X-ray image must achieve a sufficient performance level based on the image contrast, which reflects the differences in the total amount of X-ray attenuation in one direction. Using the Z_{eff} image, we can derive novel Z_{eff} information based on the same information employed to produce a conventional X-ray image. We expect that this method will contribute greatly to the use of X-rays in medicine and industry as quantitative evaluation indexes. In order to demonstrate the possible application of our image generation method, we present an image produced using fishes in Fig. 12, where the upper, middle, and low panels in the figure show the original photographs, Z_{eff} images, and conventional X-ray images, respectively. The differences between freshwater and saltwater fishes are evident in the upper and lower photographs. The conventional X-ray image shows the bone structure of both fishes as white because the X-ray path that includes bone results in high X-ray attenuation, and thus the image density decreases. The images show that the freshwater fish has a large gas bladder, as indicated in black, where the X-ray path containing the gas bladder results in less X-ray attenuation, and thus the image density increases. Compared with conventional X-ray images, the Z_{eff} images can detect unique trends. In the Z_{eff} image, the bone structure is also clearly observed with high Z_{eff} values. In addition, a dense area of high Z_{eff} values is visible around the head in the saltwater fish compared with the freshwater fish, which is only detected in the Z_{eff} image. However, the gas bladder is not visible in the Z_{eff} image because the air region contributes little to X-ray attenuation and the influence of the air region does not contribute significantly to the calculation of Z_{eff}. This is very important for understanding an Z_{eff} image. In particular, it is important to understand that the Z_{eff} image is not a coloration of a conventional X-ray image and that the color reflects the physical phenomenon of X-ray attenuation. Based on evaluations of the image from a physical perspective, it is possible to extract various types of useful information. Moreover, we consider that our system is readily applicable to current applications because our system can also produce a conventional X-ray image for standard evaluations. If the evaluator prefers to conduct quantitative analyses, the Z_{eff} image will provide further information in addition to the conventional X-ray image. This is a similar approach to dual-energy computed tomography where a novel diagnostic image [Goodsitt et al., 2011, Qu et al., 2011, Tatsugami et al., 2014] is produced in addition to the conventional computed tomography image.

4.4 Limitations

Our method produced Z_{eff} images with an accuracy of ± 0.5 Z_{eff} regardless of ρt, except for the aluminum sample with ρt = 10.0 g/cm^2, where we obtained Z_{eff} = 11.1 for this sample but the true Z_{eff} value is 13.0, as shown in Fig. 10. In the following, we explain why our ERPCD cannot accurately analyze some aluminum samples. In the experimental setup presented in Fig. 10, the aluminum sample with ρt = 10.0 g/cm^2 was exposed to air when placed on the stage and it is considered that the analysis method could not be applied in this specific situation where the conditions were assumed in advance. We deduced that the aluminum sample with ρt = 10.0 g/cm^2 resulted in extremely high X-ray attenuation compared with the other samples, and the difference in the counts between the pixels corresponding to the sample and the adjacent air region was extremely large. In this study, we reproduced the detector response under the assumption that an equilibrium is established for the secondary X-rays produced between the pixels. However, we consider that the experimental conditions for the aluminum sample with ρt = 10.0 g/cm^2 did not satisfy the required analytical conditions. To confirm this hypothesis, we performed an additional experiment where we masked the air region adjacent to the aluminum sample with ρt = 10.0 g/cm^2 using lead and a true value was obtained for the aluminum sample of Z_{eff} = 13.0.

We aim to solve this problem in the near future, but we consider that the current analytical procedure can be applied in the development of novel clinical and industrial equipment when appropriate limits are used. For example, in an actual clinical situation, it is rare to take an X-ray photograph of aluminum with a ρt greater than 10.0 g/cm^2 without the presence of adjacent materials, and aluminum with ρt = 10.0 g/cm^2 is equivalent to 6.7 cm of bone. Moreover, dental radiography is a target medical application and ρt is approximately 2.0–3.0 g/cm^2 for a tooth, which is within the applicable range of our method at present.

The degrading effects of pulse pile-up were not modeled in this study. When technological innovations that correct these effects are developed in the future, we expect that the principle of our Z_{eff} determination method will be applicable in various fields such as medicine, industry, and research.

5. Conclusions

In this study, we proposed a novel Z_{eff} determination method that uses a multi-pixel type ERPCD with three energy bins. Our method focuses on the attenuation factors (μt) of two different energy bins, and we developed an analytical procedure for deriving Z_{eff} based on the relationship between the normalized μ and reference Z_{eff} value was used. To precisely analyze Z_{eff}, we correct for the beam hardening effect and response function of the multi-pixel type ERPCD. The detector response includes the interactions between the incident X-rays and detector materials, charge sharing effect, and energy resolution. In order to demonstrate the utility of our method, the following samples were measured: acrylic (Z_{eff} = 6.5), aluminum (Z_{eff} = 13.0), and bilayer structures of acrylic and aluminum (Z_{eff} = 10.5, 9.5, and 8.5). Z_{eff} images were produced with an accuracy of Z_{eff} ± 0.5 regardless of ρt. We found that the corrections for the beam hardening effect and detector response can contribute greatly to the accurate derivation of Z_{eff}. Our method can estimate Z_{eff} for an object by correcting for both effects and it will play an important role in establishing quantitative X-ray images using ERPCD systems.

References

Alvarez R.E., Macovski A., 1976. Energy-selective reconstructions in X-ray computerized tomography. Phys Med Biol. 21(5), 733–744. doi:10.1088/0031-9155/21/5/002.

Birch R., Marshall M., 1979. Computation of bremsstrahlung x-ray spectra and comparison with spectra measured with a Ge (Li) detector. Phys Med Biol. 24(3), 505–517.

Brooks R.A., Di Chiro G., 1976. Beam hardening in x-ray reconstructive tomography. Phys Med Biol. 21(3), 390–398.

Dong X., et al., 2019. An improved physics model for multi-material identification in photon counting CT. Proc SPIE 10948, Med Imaging. 109484O. doi: 10.1117/12.2512525.

Dreier E.S., et al., 2018. Spectral correction algorithm for multispectral CdTe x-ray detectors. Opt Eng. 57(5), 054117-1–13. doi:10.1117/1.OE.57.5.054117.

Fredenberg E., et al., 2013. Measurement of breast-tissue x-ray attenuation by spectral mammography: first results on cyst fluid. Phys Med Biol. 58(24), 8609–8620. doi:10.1088/0031-9155/58/24/8609.

Goodsitt M.M., et al., 2011. Accuracies of the synthesized monochromatic CT numbers and effective atomic numbers obtained with a rapid kVp switching dual energy CT scanner. Med Phys. 38(4), 2222–2232. doi:10.1118/1.3567509.

Hayashi H., et al., 2021. Photon Counting Detectors for X-ray Imaging: Physics and Applications. Springer, 1–148. ISBN-10: 3030626792.

Hayashi H., et al., 2017. Response functions of multi-pixel-type CdTe detector -Toward development of precise material identification on diagnostic X-ray images by means of photon counting-. Proc SPIE 10132, Med Imaging. 1013236-1–18. doi:10.1117/12.2251185.

Hirayama H., Namito Y., 2005. The EGS5 code system. KEK Report, 1–418.

Hsieh S.S., et al., 2018. Spectral resolution and high-flux capability tradeoffs in CdTe detectors for clinical CT. Med Phys. 45(4), 1433–1443. doi:10.1002/mp.12799.

Hubbell J.H., 1982. Photon mass attenuation and energy-absorption coefficients. Int J Appl Radiat Isot. 33(11), 1269–1290. doi:10.1016/0020-708X(82)90248-4.

Iramina H., et al., 2018. Effective Atomic Number Measurement with Energy-Resolved Computed Tomography Using Two-Dimensional “transXend” Detector. Int. J. Medical Physics, Clinical Engineering and Radiation Oncology. 7, 61–73. doi: 10.4236/ijmpcero.2018.71006.

Kimoto N., et al., 2017. Precise material identification method based on a photon counting technique with correction of the beam hardening effect in X-ray spectra. Appl Radiat Isot. 124, 16–26. doi:10.1016/j.apradiso.2017.01.049.

Kimoto N., et al., 2018. Reproduction of response functions of a multi-pixel-type energy-resolved photon counting detector while taking into consideration interaction of X-rays, charge sharing and energy resolution. IEEE Nuclear Science Symposium and Medical Imaging Conference (NSS/MIC), 1–4. doi: 10.1109/NSSMIC.2018.8824417.

Kimoto N., et al., 2019. Feasibility study of photon counting detector for producing effective atomic number image. 2019 IEEE Nuclear Science Symposium and Medical Imaging Conference (NSS/MIC), 1–4. doi: 10.1109/NSS/MIC42101.2019.9059919.

Knoll G.F., 2000. Radiation detection and measurement. John Wiley & Sons, New York, 1–802.

Korner M., et al., 2007. Advances in digital radiography: physical principles and system overview. Radiographics. 27(3), 675–686. doi:10.1148/rg.273065075

Leng S., et al., 2019. Photon-counting Detector CT: System Design and Clinical Applications of an Emerging Technology. Radiographics. 39(3), 729–743. doi:10.1148/rg.2019180115.

Maeda K., et al., 2005. Compton-scattering measurement of diagnostic x-ray spectrum using high-resolution Schottky CdTe detector. Med Phys. 32(6), 1542–1547. doi: 10.1118/1.1921647.

Otfinowski P., 2018. Spatial resolution and detection efficiency of algorithms for charge sharing compensation in single photon counting hybrid pixel detectors. Nucl Instrum Methods Phys Res, Sect A. 882, 91–95. doi:10.1016/j.nima.2017.10.092.

Park K., et al., 2018. Improvement of spatial resolution in a Timepix based CdTe photon counting detector using ToT method. Nucl Instrum Methods in Phys Res Sect A. 891, 18–24. doi:10.1016/j.nima.2018.02.050.

Qu M., et al., 2011. Dual-energy dual-source CT with additional spectral filtration can improve the differentiation of non-uric acid renal stones: an ex vivo phantom study. AJR Am J Roentgenol. 196(6), 1279–1287. doi:10.2214/AJR.10.5041.

Reza S., et al., 2017. Semiconductor radiation detectors: technology and applications. CRC Press, New York, 1–290.

Rinkel J., et al., 2011. Experimental evaluation of material identification methods with CdTe X-ray spectrometric detector. IEEE Transactions on Nuclear Science. 58(5), 2371–2377. doi: 10.1109/TNS.2011.2164266.

Rowlands J.A., 2002. The physics of computed radiography. Phys Med Biol. 47(23), R123–R166. doi:10.1088/0031-9155/47/23/201.

Sasaki M., et al., 2019. A novel mammographic fusion imaging technique: the first results of tumor tissues detection from resected breast tissues using energy-resolved photon counting detector. Proc SPIE 10948, Med Imaging, 1094864. doi:10.1117/12.2512271.

Samei E., Flynn M.J., 2003. An experimental comparison of detector performance for direct and indirect digital radiography systems. Med Phys. 30(4), 608–622. doi:10.1118/1.1561285.

Scheiber C., Giakos C.G., 2001. Medical applications of CdTe and CdZnTe detectors. Nucl Instrum Methods Phys Res, Sect A. 458, 12–25. doi: 10.1016/S0168-9002(00)01032-9.

Sellerer T., et al., 2019. Quantitative dual-energy micro-CT with a photon-counting detector for material science and non-destructive testing. PLoS ONE. 14(7), 1–18. doi: 10.1371/journal.pone.0219659.

Spekowius G., Wendler T., 2006. Advances in healthcare technology: shaping the future of medical care. Springer, Netherlands, 49–64.

Spiers F.W., 1946. Effective atomic number and energy absorption in tissues. Br J Radiol. 19(218), 52–63. doi:10.1259/0007-1285-19-218-52.

Taguchi K., Iwanczyk J.S., 2013. Vision 20/20: single photon counting x-ray detectors in medical imaging. Med Phys. 40(10), 100901-1–19. doi:10.1118/1.4820371.

Taguchi K., et al., 2018. Spatio-energetic cross-talk in photon counting detectors: Numerical detector model (PcTK) and workflow for CT image quality assessment. Med Phys. 45(5), 1985–1998. doi:10.1002/mp.12863.

Tatsugami F., et al., 2014. Measurement of electron density and effective atomic number by dual-energy scan using a 320-detector computed tomography scanner with raw data-based analysis: a phantom study. J Comput Assist Tomogr. 38(6), 824–827. doi: 10.1097/RCT.0000000000000129.

Trueb P., et al., 2017. Assessment of the spectral performance of hybrid photon counting x-ray detectors. Med Phys. 44(9), e207–e214. doi:10.1002/mp.12323.

Wang X., et al., 2011. Material separation in x-ray CT with energy resolved photon-counting detectors. Med Phys. 38(3), 1534–1546. doi:10.1118/1.3553401.

Willemink M.J., et al., 2018. Photon-counting CT: Technical Principles and Clinical Prospects. Radiology. 289(2), 293–312. doi:10.1148/radiol.2018172656.

Yamashita Y., et al., 2014. Measurement of effective atomic numbers using energy-resolved computed tomography. Journal of Nuclear Science and Technology. 51(10), 1256–1263. doi: 10.1080/00223131.2014.919881.

Zambon P., et al., 2018. Spectral response characterization of CdTe sensors of different pixel size with the IBEX ASIC. Nucl Instrum Methods Phys Res, Sect A. 892, 106–113. doi: 10.1016/j.nima.2018.03.006.

Figures

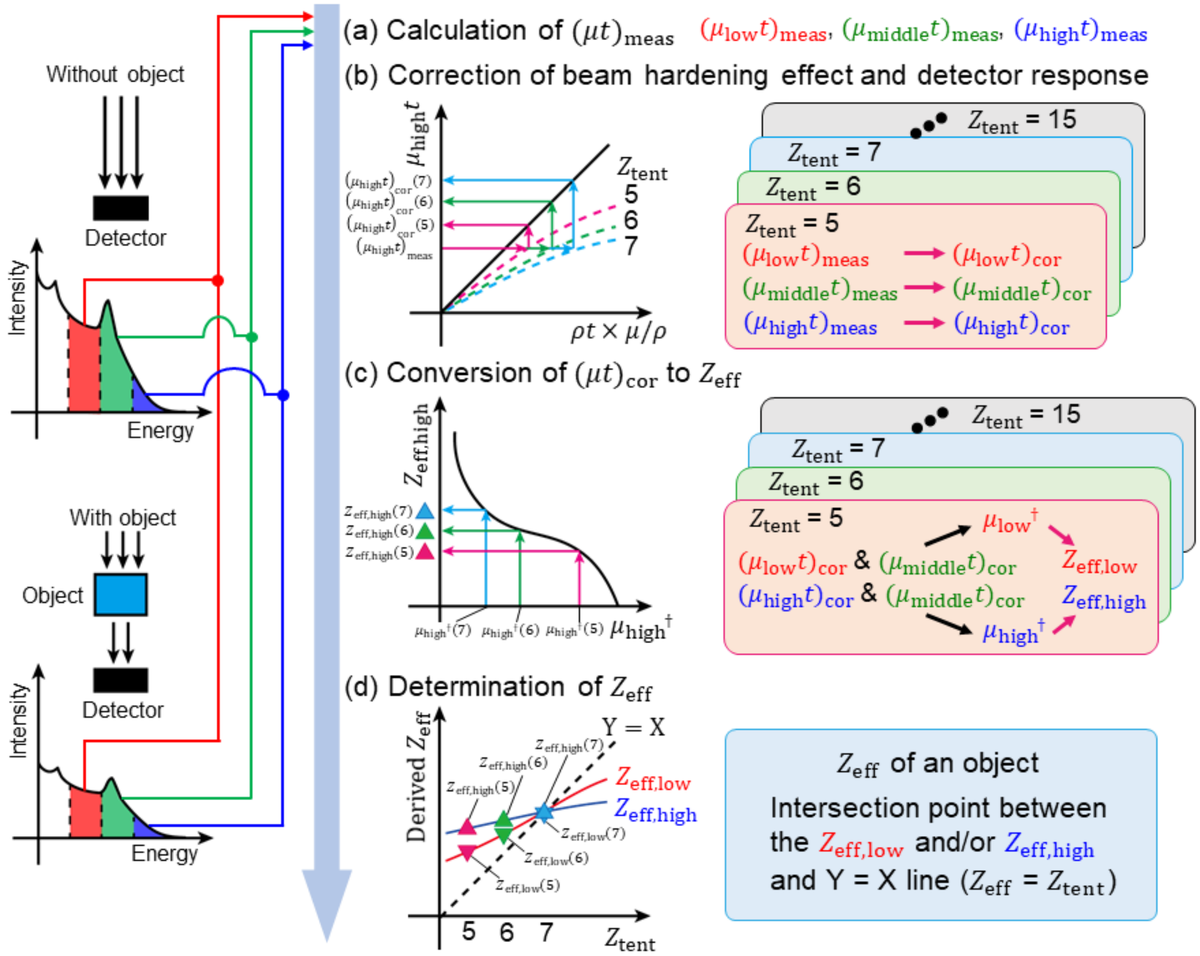

Fig. 1 Schematic illustration of the procedure for determining the effective atomic number (Z_{eff}) by considering the beam hardening effect and detector response. First, as presented in the left panel, the X-ray spectra with and without objects are measured using an ERPCD with three different energy bins. The intensities of each energy bin are applied in procedures (a) to (d). (a) Calculation of the measured attenuation factor $(\mu t)_{meas}$ for each energy bin; $(\mu_{low}t)_{meas}$, $(\mu_{middle}t)_{meas}$, and $(\mu_{high}t)_{meas}$ correspond to the low, middle, and high energy bins, respectively. (b) Correction of $(\mu t)_{meas}$. Using a tentatively determined atomic number, Z_{tent}, $(\mu t)_{meas}$ is corrected to $(\mu t)_{cor}$, and the beam hardening effect and detector response are corrected. The analysis is conducted based on Z_{tent} values of 5.0–15.0. (c) Conversion of $(\mu t)_{cor}$ to Z_{eff}. Using $(\mu_{high}t)_{cor}$ and $(\mu_{middle}t)_{cor}$, $Z_{eff,high}$ is derived based on the theoretical relationship between the normalized linear attenuation coefficient $\mu_{high}^{\dagger}$ and Z_{eff}. In a similar manner, $Z_{eff,low}$ is derived from $\mu_{low}^{\dagger}$, which is calculated from $(\mu_{low}t)_{cor}$ and $(\mu_{middle}t)_{cor}$. (d) Determination of Z_{eff}. Based on the relationship between the derived Z_{eff} values ($Z_{eff,low}$ and/or $Z_{eff,high}$) and Z_{tent}, Z_{eff} is determined for an object from the intersection point of the Y = X line and $Z_{eff,low}$ and/or $Z_{eff,high}$ curves.

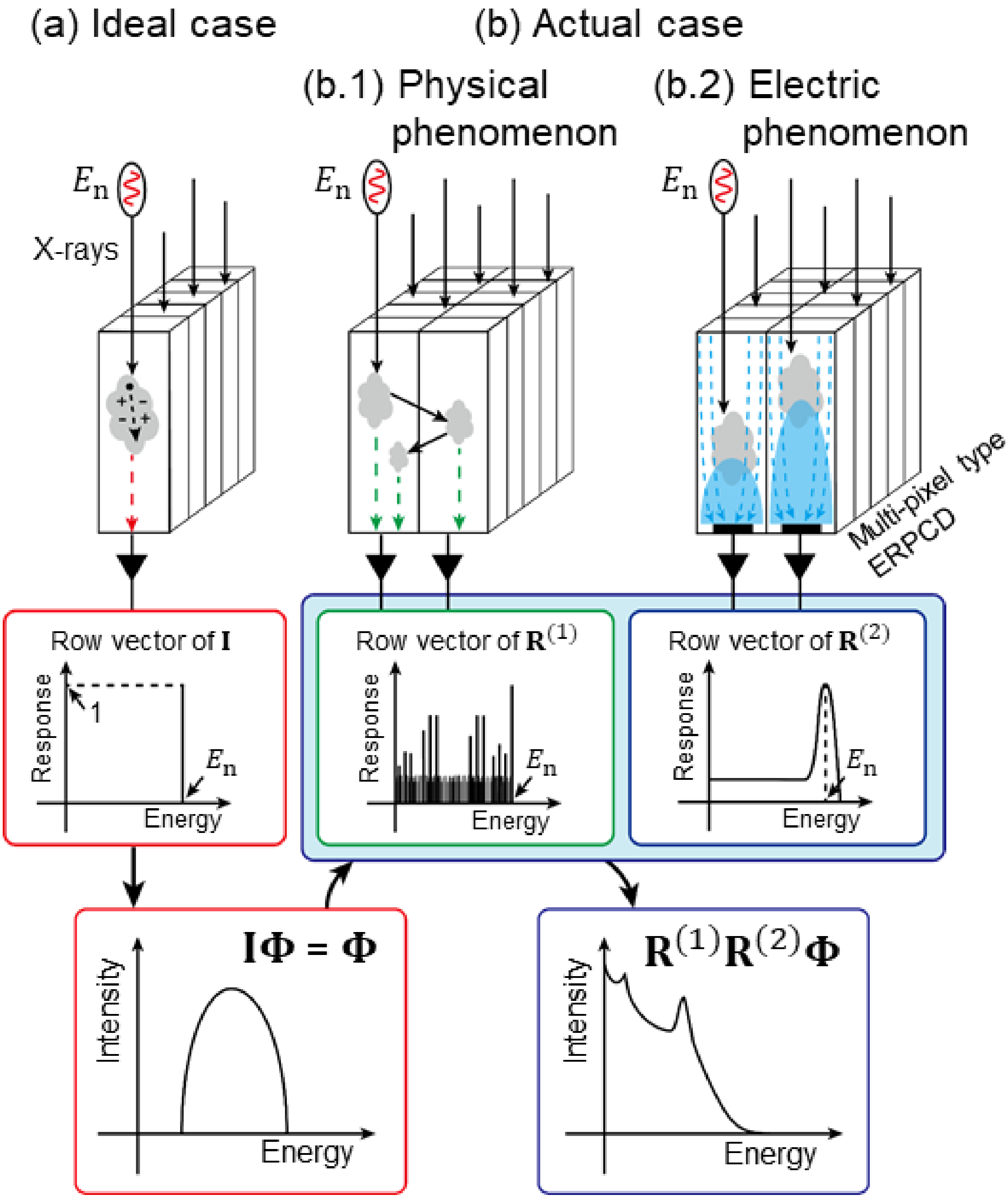

Fig. 2 Schematic illustration of the X-ray spectrum measured with a multi-pixel type ERPCD. (a) Ideal situation where only full energy absorption occurs. In this case, the ideal X-ray spectrum $\mathbf{\Phi}$ is obtained by calculating $\mathbf{I\Phi}$ because the response function $\mathbf{I}$ involves full energy absorption. (b) Actual situation where the X-ray spectrum measured with a multi-pixel type ERPCD can be reproduced by $\mathbf{R}^{(1)}\mathbf{R}^{(2)}\mathbf{\Phi}$. These responses are represented by $\mathbf{R}^{(1)}$ and $\mathbf{R}^{(2)}$. $\mathbf{R}^{(1)}$ considers the transportation of secondary X-rays produced via the interactions between incident X-rays and the detector materials, as shown in (b.1). $\mathbf{R}^{(2)}$ is the charge transportation, as shown in (b.2).

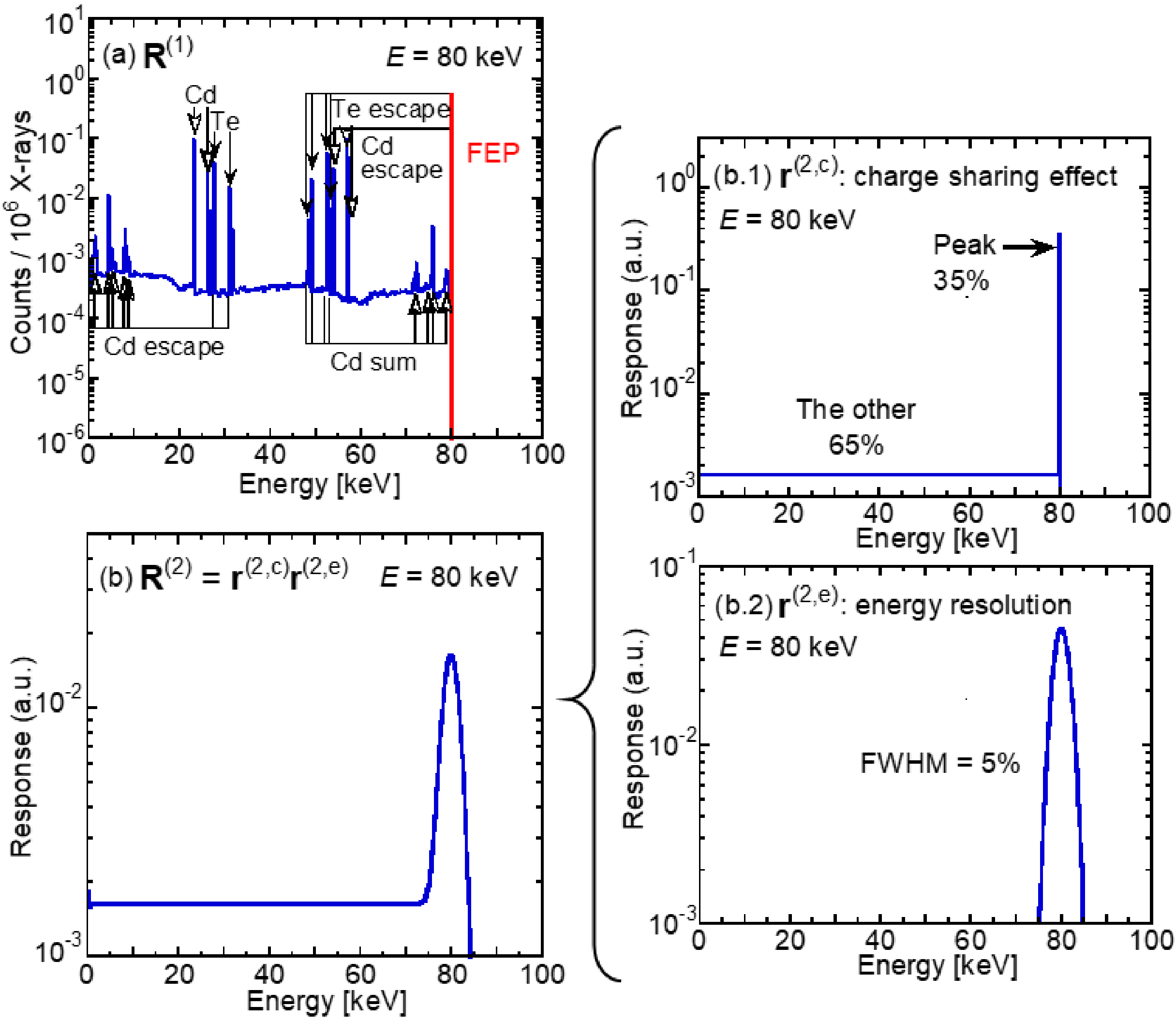

Fig. 3 Typical results for response functions of 80-keV monochromatic X-rays. (a) Response function $\mathbf{R}^{(1)}$ based on the physical interaction between incident X-rays and detector materials. $\mathbf{R}^{(1)}$ is calculated by Monte-Carlo simulation. (b) Response function $\mathbf{R}^{(2)}$ comprising the charge sharing effect $\mathbf{r}^{(2,c)}$ and energy resolution $\mathbf{r}^{(2,e)}$, which are shown in (b.1) and (b.2), respectively. Parameters for $\mathbf{r}^{(2,c)}$ and $\mathbf{r}^{(2,e)}$ are optimized in order to reproduce the X-ray spectrum measured with our ERPCD system.

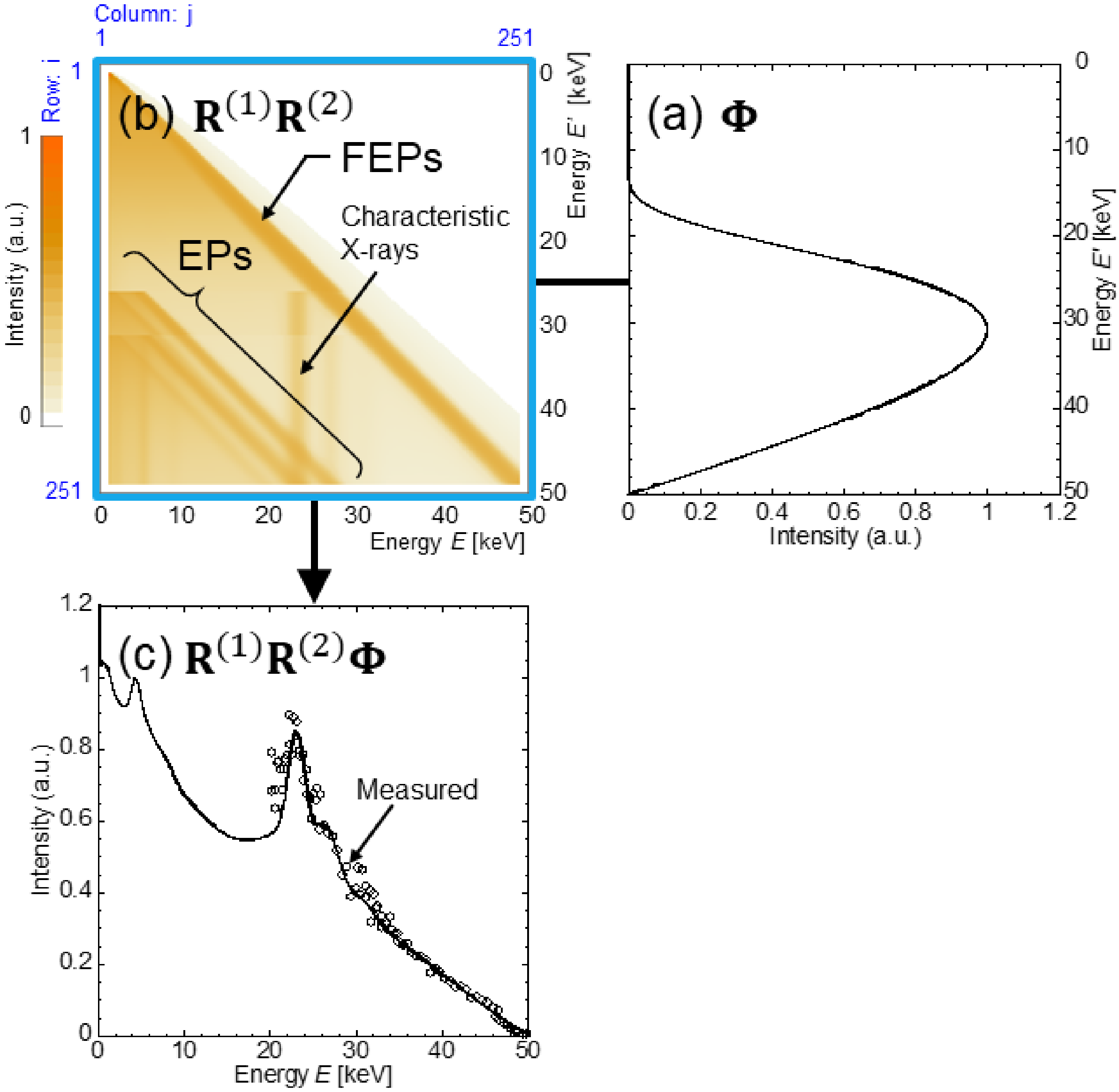

Fig. 4 Schematic illustration of the procedure for reproducing the X-ray spectrum obtained by a multi-pixel type ERPCD. (a) Ideal X-ray spectrum $\mathbf{\Phi}$. (b) Color maps of the $\mathbf{R}^{(1)}\mathbf{R}^{(2)}$ matrix. (c) Reproduced X-ray spectrum $\mathbf{R}^{(1)}\mathbf{R}^{(2)}\mathbf{\Phi}$, where the open circle denotes experimental data, and $\mathbf{R}^{(1)}\mathbf{R}^{(2)}\mathbf{\Phi}$ is in good agreement with the experimental data.

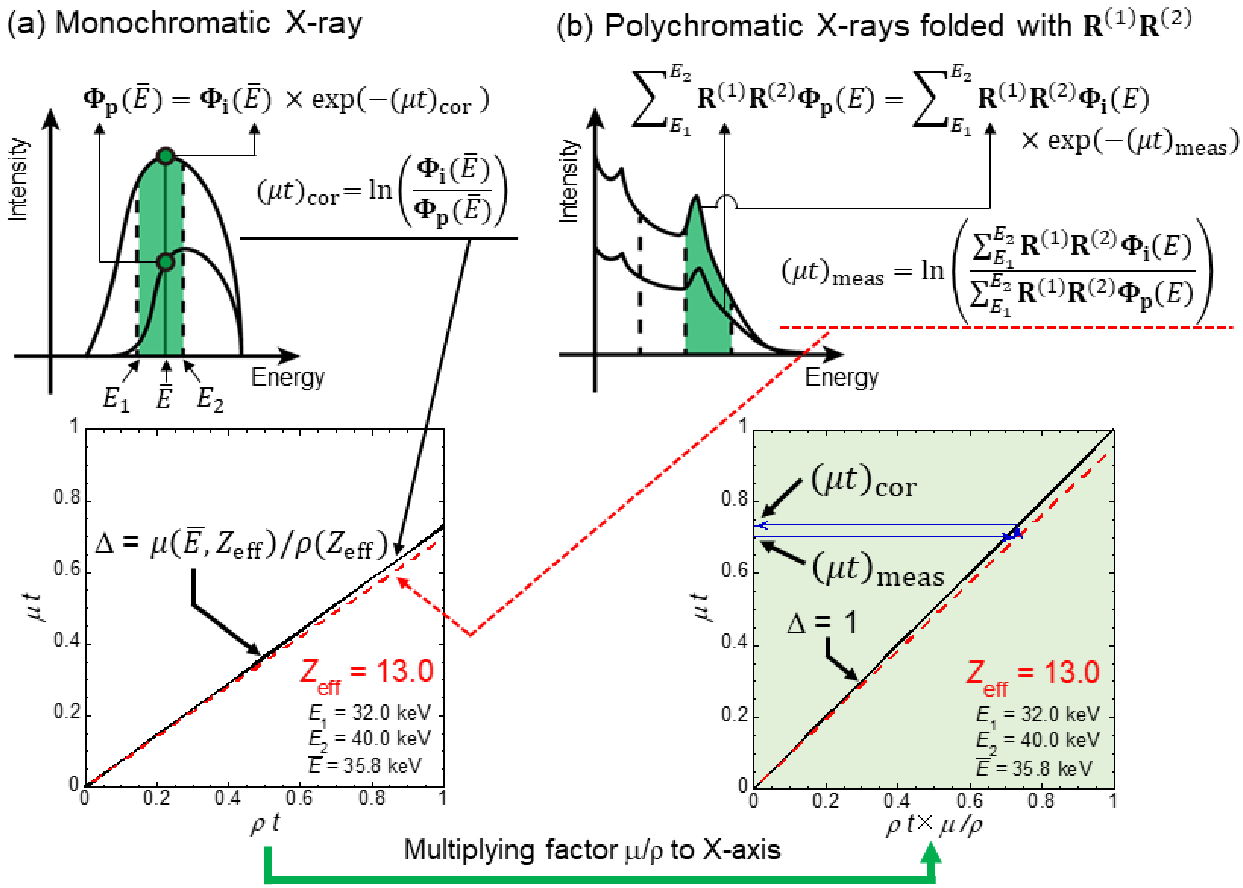

Fig. 5 Schematic illustration of the procedure used to correct for the beam hardening effect and detector response. (a) Procedure for calculating the ideal attenuation factor $(\mu t)_\mathrm{cor}$ derived from monochromatic X-rays, where we focus on the mean energy weighted using a spectrum $\mathbf{\Phi}$. (b) Corresponding measured attenuation factor $(\mu t)_\mathrm{meas}$ derived from $\mathbf{R}^{(1)}\mathbf{R}^{(2)}\mathbf{\Phi}$. In the plot of the mass thickness ρt versus μt presented in the lower left panel, the gradient of the monochromatic X-ray is μ/ρ for an object. In order to perform the correction clearly, standardization is performed by multiplying μ/ρ to the X-axis. The relationship between $\rho t \times \mu/\rho$ $(= \mu t)$ and μt is presented in the lower right panel, where the gradient of the monochromatic X-ray is 1 regardless of Z_eff. The correction procedure is denoted by blue arrows. The experimentally obtained $(\mu t)_\mathrm{meas}$ can be converted into $(\mu t)_\mathrm{cor}$. This process can simultaneously correct for the beam hardening effect and detector response.

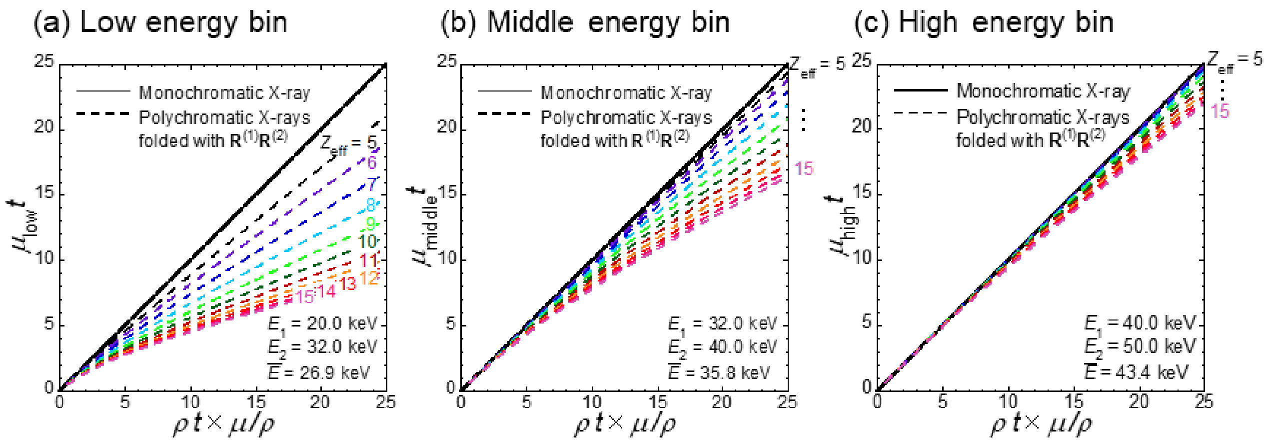

Fig. 6 Corrections curve for μt values for three energy bins, where (a), (b), and (c) are the low, middle, and high energy bins, respectively. The solid line and broken curves correspond to a monochromatic X-ray based on $\mathbf{\Phi}$ and polychromatic X-rays folded with $\mathbf{R}^{(1)}\mathbf{R}^{(2)}$, respectively. The correction amount is the difference between the monochromatic X-ray and polychromatic X-rays, and it depends on Z_{eff}. Correction can be conducted for both the beam hardening effect and detector response using this relationship.

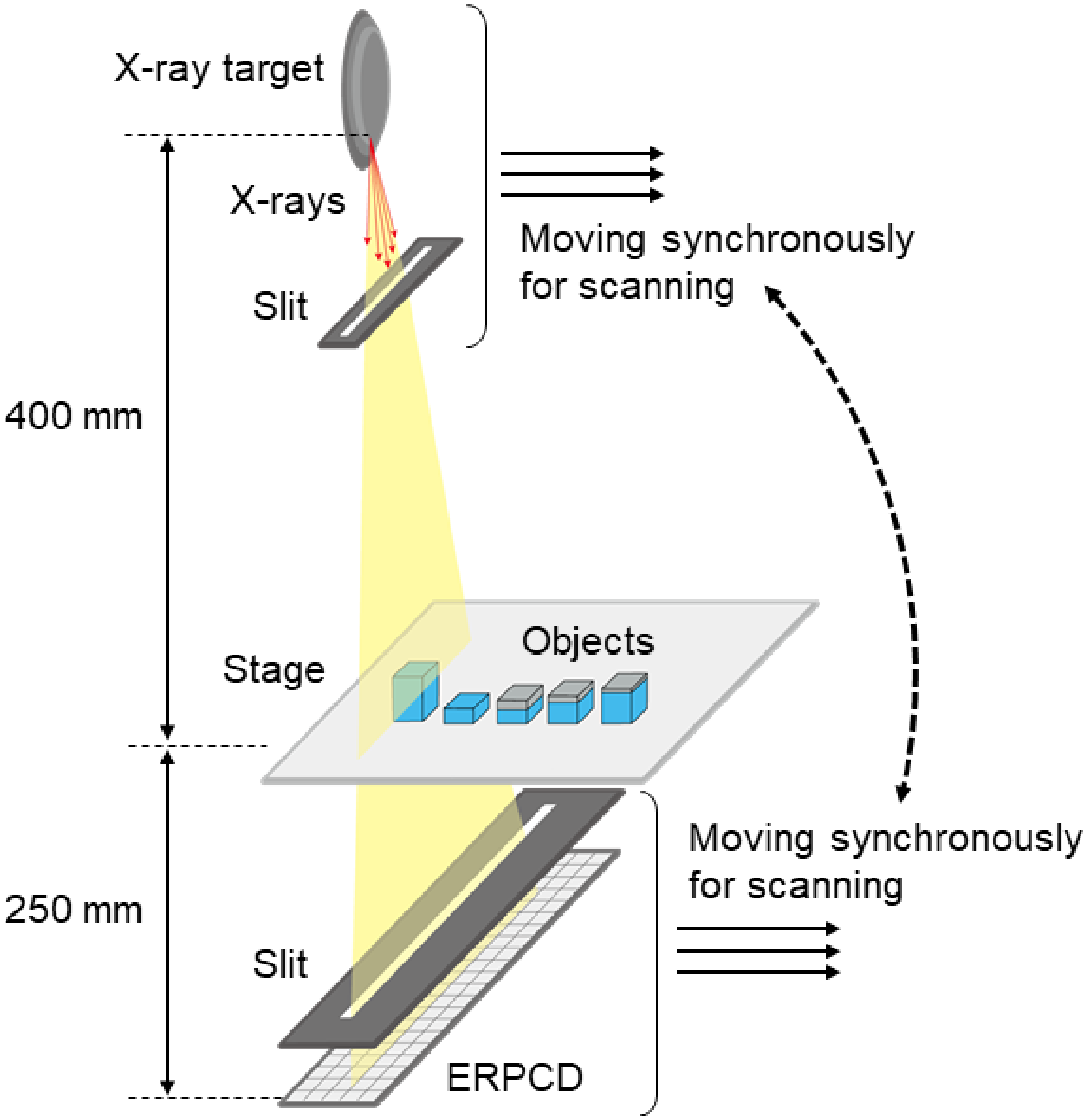

Fig. 7 Schematic illustration of the experimental setup. A multi-pixel type ERPCD was installed in a slit scanning system.

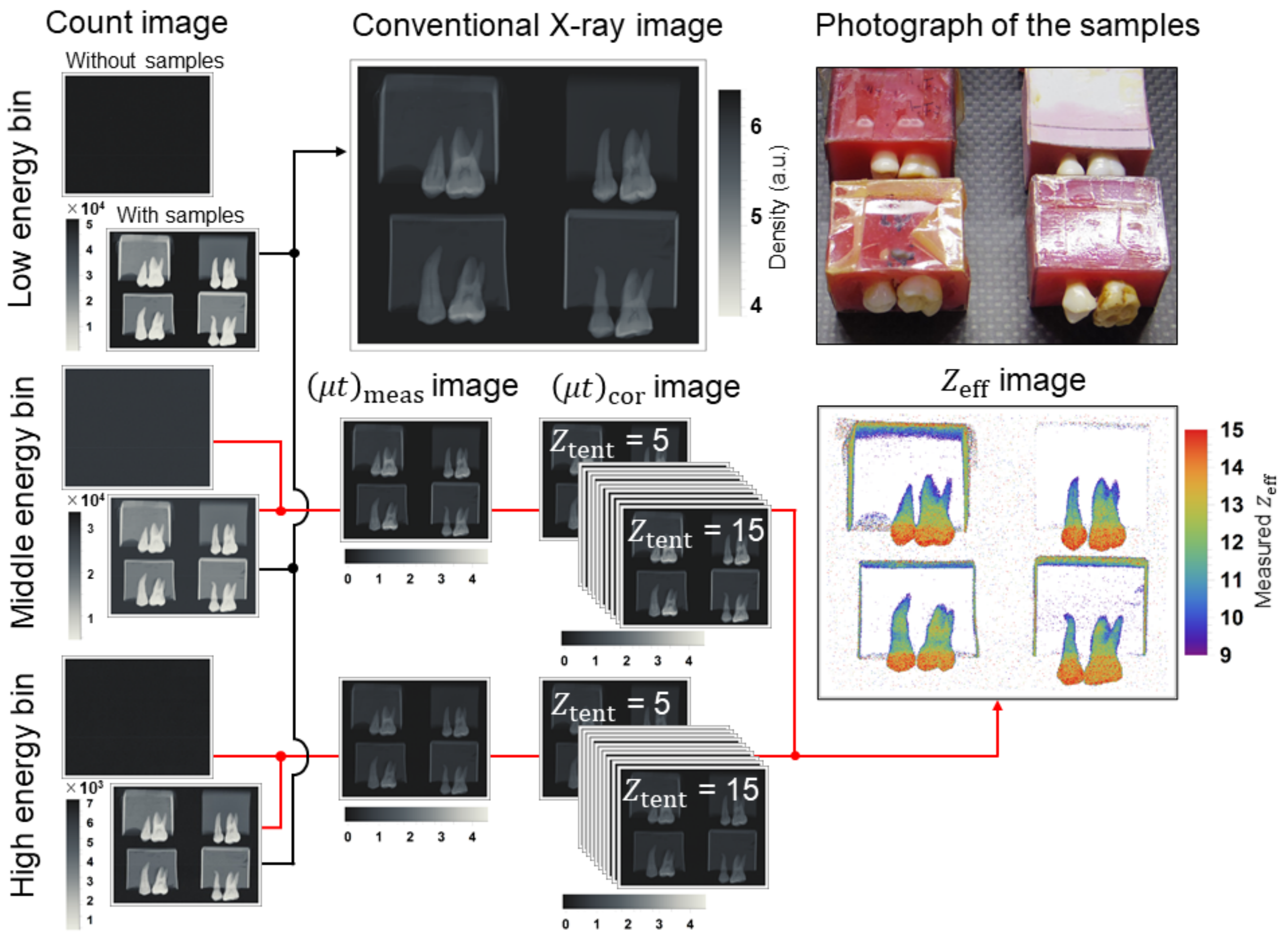

Fig. 8 Diagram showing the proposed X-ray imaging system. Our system can produce a conventional X-ray image and an Z_{eff} image based on the same data. Count images for three energy bins with and without the presence of a sample were prepared as shown in the left panel. First, count images of three energy bins with the sample present were analyzed and a conventional X-ray image was produced, as shown by the black arrow. Next, the count images with and without the presence of the sample were analyzed for the middle and high energy bins in the direction shown by the red arrows, and an Z_{eff} image with a color scale was derived.

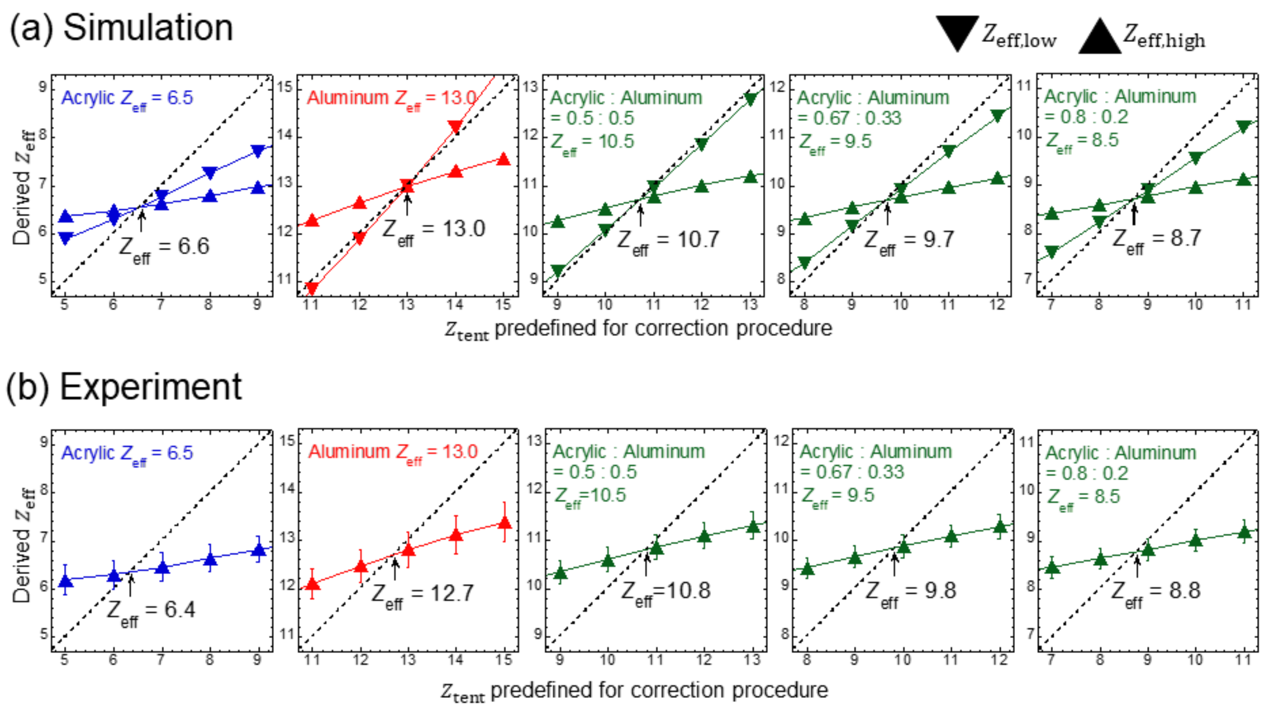

Fig. 9 Comparison of Z_{eff} determination in (a) simulations and (b) experiments. $Z_{\mathrm{eff,low}}$ (lower triangle) and $Z_{\mathrm{eff,high}}$ (upper triangle) are plotted as a function of Z_{tent}, which was tentatively set based on the correction for the beam hardening effect and detector response. The blue and red closed triangles correspond to acrylic and aluminum samples, respectively. The green open triangles denote bilayer structures of acrylic and aluminum, where the ratio of acrylic relative to aluminum varied as shown: 0.5:0.5, 0.67:0.33, and 0.8:0.2. The results for ρt = 5.0 g/cm^2 are presented. Z_{eff} was determined based on the intersection point of the $Z_{\mathrm{eff,high}}$ curve and Y = X line, and the values are in good agreement with the theoretical values. By contrast, it is difficult to identify an intersection point using $Z_{\mathrm{eff,low}}$. The experimental Z_{eff} values agree well with the simulated values, thereby demonstrating that our method can determine Z_{eff} in an appropriate manner.

Condition	(a) ρt = 1.0 g/cm^2					(b) ρt = 5.0 g/cm^2					(c) ρt = 10.0 g/cm^2				
Thickness of acrylic [mm]	8.4	0	4.2	5.6	6.7	42.0	0	21.0	28.0	33.6	84.0	0	42.0	56.0	67.2
Thickness of aluminum [mm]	0	3.7	1.9	1.2	0.7	0	18.5	9.3	6.2	3.7	0	37.1	18.5	12.4	7.4
Photograph	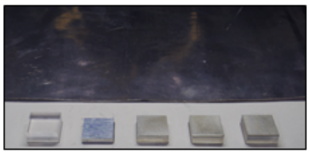					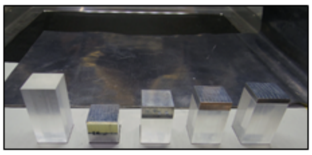					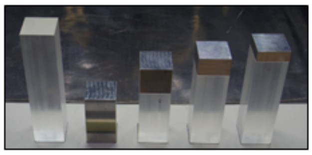				
Conventional X-ray image															
Z_{eff} image															
Derived Z_{eff}#	6.1	12.9	10.9	9.6	8.4	6.4	12.7	10.8	9.8	8.8	6.5	11.1	10.4	9.6	8.6
Theoretical Z_{eff}	6.5	13.0	10.5	9.5	8.5	6.5	13.0	10.5	9.5	8.5	6.5	13.0	10.5	9.5	8.5

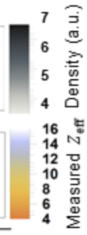

The mean values within and outside a range of ± 0.5 from the theoretical Z_{eff} are shown in blue and red, respectively.

Fig. 10 Results for images produced using samples with different ρt values, where (a), (b), and (c) correspond to 1.0, 5.0, and 10.0 g/cm^2, respectively. In each image, the acrylic, aluminum, and bilayer structures are arranged in order from left to right. We measured objects with well-known Z_{eff} values, where the theoretical Z_{eff} values for these objects are 6.5, 13.0, 10.5, 9.5, and 8.5 regardless of ρt. The middle images are conventional X-ray images. The bottom images are Z_{eff} images and the ROI is shown in each figure. The bottom row shows the mean Z_{eff} value in the ROI. The mean values within a range of ± 0.5 from the theoretical Z_{eff} are shown in blue, and those outside a range of ± 0.5 from the theoretical Z_{eff} are shown in red. The Z_{eff} image was obtained with an accuracy of ± 0.5, except for aluminum with ρt = 10 g/cm^2.

Condition	(a)		(b)		(c)	
Beam hardening	Not corrected		Corrected		Corrected	
Detector response	Not corrected		Not corrected		Corrected	
Z_{eff} image						
Derived Z_{eff}#	5.9	10.0	5.9	10.3	6.4	12.7
Theoretical Z_{eff}	6.5	13.0	6.5	13.0	6.5	13.0

The mean values within and outside a range of ± 0.5 from the theoretical Z_{eff} are shown in blue and red, respectively.

Fig. 11 Illustration of the importance of correcting for the beam hardening effect and detector response. The left and right images correspond to acrylic (Z_{eff} = 6.5) and aluminum (Z_{eff} = 13.0), respectively. Z_{eff} images: (a) without correcting for both the beam hardening effect and detector response, (b) with correction for the beam hardening effect, and (c) with correction for both the beam hardening effect and detector response. As shown in (a) and (b), the mean values of both samples are not in agreement with the theoretical values. However, after correcting for both effects, the results for the acrylic and aluminum samples are in good agreement with the theoretical values. Clearly, correction should be made for the beam hardening effect and detector response to accurately derive Z_{eff}.

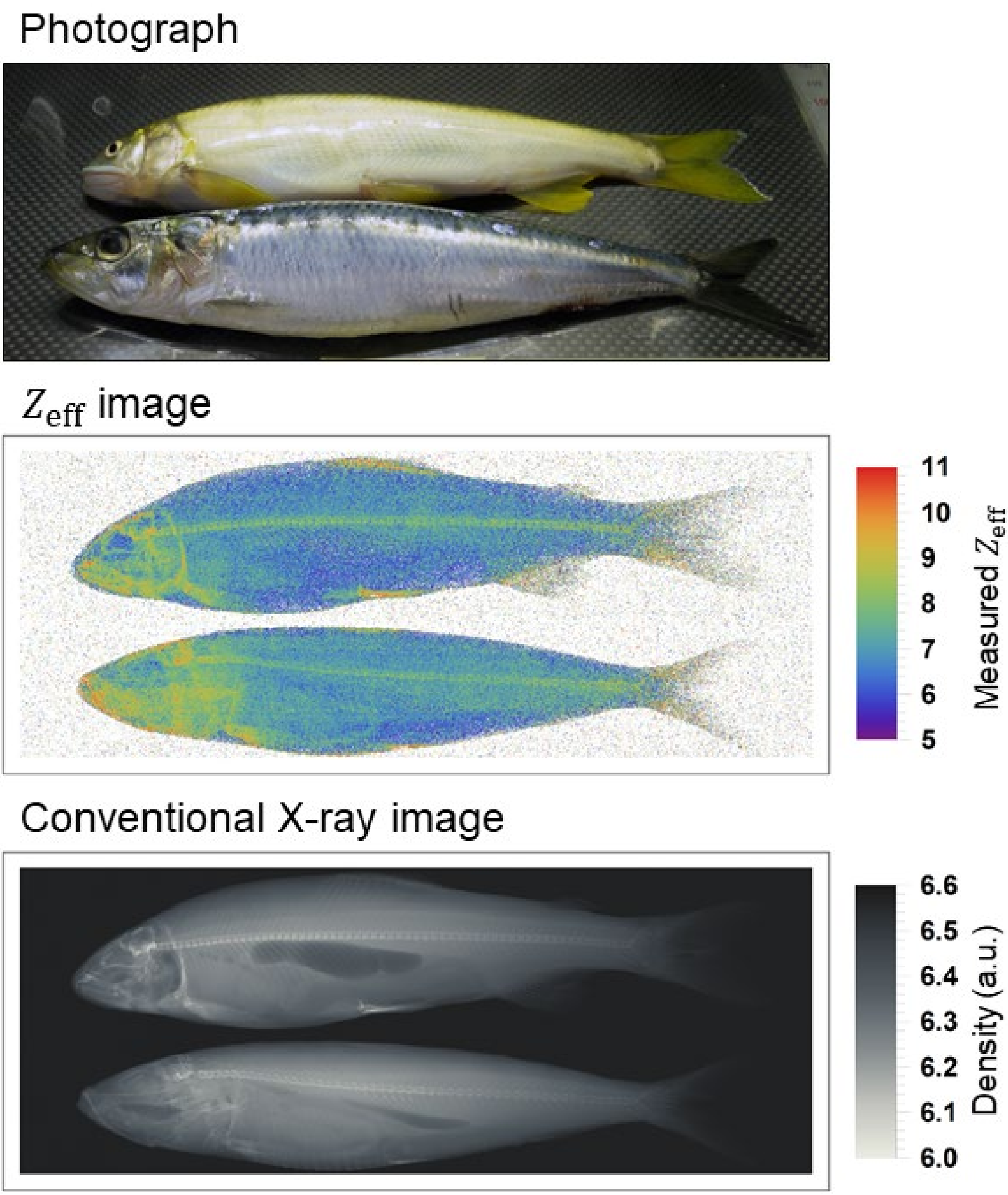

Fig. 12 Derivation of novel information by using Z_{eff} images of fish samples. The upper and lower images in each figure are of a freshwater fish and saltwater fish, respectively. The upper, middle, and low figures show photographs, Z_{eff} images, and conventional X-ray images, respectively. In the Z_{eff} image, the bone structure is clearly indicated by the high Z_{eff} values. In addition, a dense area with high Z_{eff} values is present around the head of the saltwater fish compared with the freshwater fish, and it can only be detected using an Z_{eff} image.